nature catalysis

Article

https://doi.org/10.1038/s41929-025-01425-3

Architecture, catalysis and regulation of methylthio-alkane reductase for bacterial sulfur acquisition from volatile organic compounds

Received: 11 October 2024

Accepted: 10 September 2025

Srividya Murali[1,7], Guo-Bin Hu[2,7], Dale F. Kreitler[3], Ana Arroyo Carriedo[1], Luke C. Lewis[4], Samuel Adu Fosu[1], Olivia G. Weaver[1], Ella M. Buzas[1], Kathryn M. Byerly[1], Yasuo Yoshikuni[5], Sean McSweeney[2,3], Hannah S. Shafaat[4,6] & Justin A. North[1] ✉

Bacteria utilize methylthio-alkane reductase (MAR) to acquire sulfur from volatile organic sulfur compounds. Reductive cleavage of methylthio-ethanol and dimethylsulfide liberates methanethiol for methionine synthesis and concomitantly releases ethylene and methane, respectively. Here we show that the native MAR of *Rhodospirillum rubrum* is a two-component system composed of a MarH ATP-dependent reductase and a MarDK catalytic core, whose architecture parallels nitrogenase. MarS complexes with MarDK to downregulate MAR activity during cellular sulfate influx, based on chromatographic and activity analyses. MarDK possesses complex metallocofactors resembling, but not identical to, nitrogenase P- and iron-only M-clusters, designated as mar1 and mar2 clusters based on metal, spectroscopic and mutagenesis analyses. They exhibit electronic features similar to the iron-only nitrogenase under turnover and, remarkably, are matured by MarB or nitrogenase NifB, resulting in maturase-dependent activity profiles. Altogether, this suggests a broader scope of reactivity, mechanisms and regulation in microbial metabolism for the nitrogenase-like family of enzymes than previously considered.

Volatile organic sulfur compounds (VOSCs) are ubiquitous in the global sulfur cycle and serve as sources of sulfur for the metabolism of many bacteria[1]. Dimethylsulfide (DMS), the most abundant VOSC on Earth, is produced by bacteria on the order of 10 teragrams of sulfur per year[2]. Other VOSCs such as methylthio-propanol and methylthio-ethanol (MT-EtOH) are produced by microbial fermentation or recycling of the amino acid methionine[3,4]. The methylthio-alkane reductase (MAR) system in anaerobic and phototrophic terrestrial bacteria such as *Rhodospirillum rubrum* and *Rhodopseudomonas palustris* was discovered to be involved in unprecedented reductive C–S bond cleavage of VOSCs to acquire sulfur. For example, cleavage of DMS and MT-EtOH resulted in methanethiol (CH_3–SH) for needed methionine biosynthesis, along with the release of methane and ethylene, respectively, as by-products[5]. This process required nitrogen fixation-like (NFL) genes *marBHDK* that had remained of unknown function for over a decade since their initial bioinformatic identification in bacterial

---

[1]Department of Microbiology, The Ohio State University, Columbus, OH, USA. [2]Brookhaven National Laboratory, Laboratory for BioMolecular Structures, National Synchrotron Light Source II, Upton, NY, USA. [3]Brookhaven National Laboratory, Center for Biomolecular Structure, National Synchrotron Lights Source II, Upton, NY, USA. [4]Department of Chemistry and Biochemistry, The Ohio State University, Columbus, OH, USA. [5]Department of Energy Joint Genome Institute, Lawrence Berkeley National Laboratory, Berkeley, CA, USA. [6]Department of Chemistry and Biochemistry, University of California, Los Angeles, Los Angeles, CA, USA. [7]These authors contributed equally: Srividya Murali, Guo-Bin Hu. ✉e-mail: north.62@osu.edu

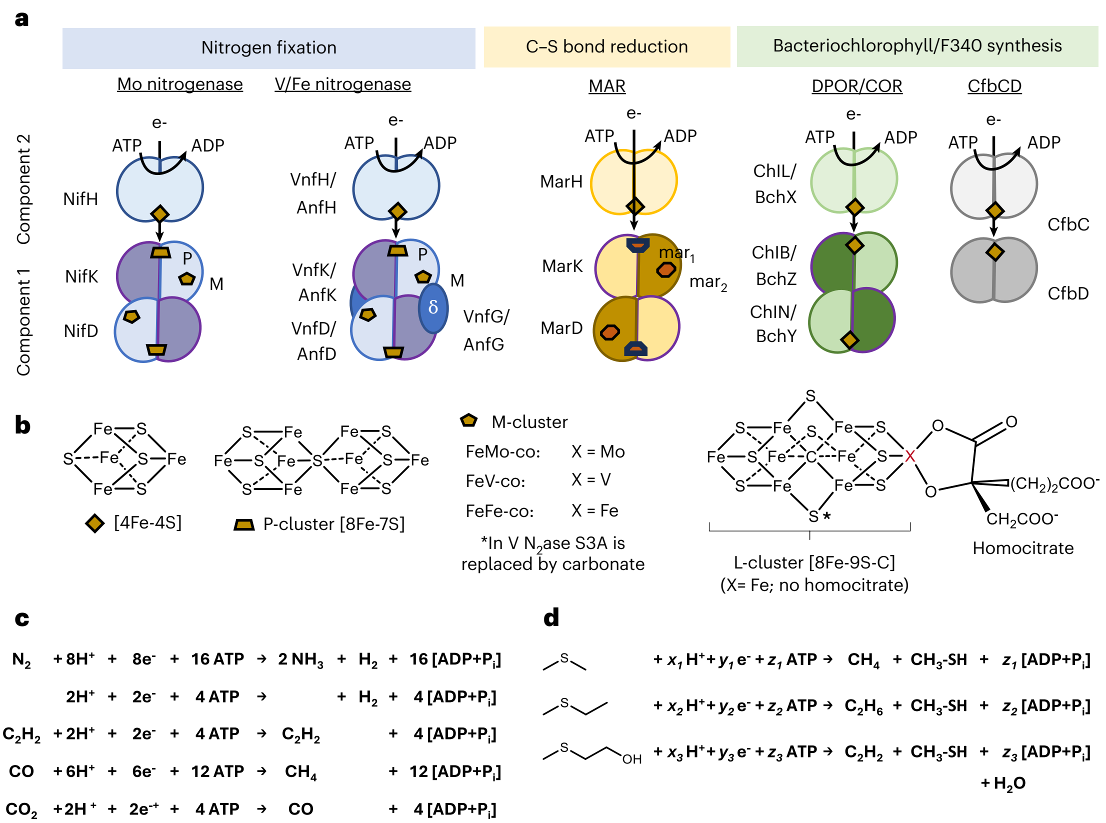

Fig. 1 | Nitrogenase and NFL systems. a,**b**, Subunit composition (**a**) and metallocofactor composition (**b**) of the three isoforms of N_2ase and the NFL systems, which are MAR for reductive C–S bond cleavage of VOSCs[5], DPOR and COR for bacteriochlorophyll synthesis[9,10] and CfbCD for methanogenesis F430 cofactor synthesis[11]. For V and Fe N_2ase, an additional G-subunit (δ) is involved in M-cluster association and interactions between components[26,48,70]. The mar1 and mar2 clusters are P-like and FeFe-co-like metallocofactors whose precise identity is not fully resolved. **c**, Reactions catalysed by N_2ase. **d**, Reactions catalysed by MAR.

genomes[3,5]. Furthermore, MAR genes were under transcriptional control of a sulfate-responsive regulator, SalR, that activated gene expression when sulfate became limiting[5]. These findings revealed that anaerobic bacteria with MAR turn to VOSCs for sulfur acquisition when sulfate is scarce. However, the structural and functional basis for reductive C–S bond cleavage by an NFL system remained unknown.

The nitrogenase superfamily of enzymes characterized so far is composed of distinct reductases involved in nitrogen, carbon and energy metabolism. Nitrogenase (N_2ase) performs essential biological nitrogen fixation by reducing N_2 to ammonia. It also reduces protons, acetylene, CO and CO_2, among other small double- and triple-bond-containing compounds[6–8] (Fig. 1). Alternately, the NFL dark-operative protochlorophyllide oxidoreductase (DPOR) and chlorophyllide oxidoreductase (COR) reduces porphyrin ring C=C double bonds for bacteriochlorophyll biosynthesis[9,10], and Ni^{2+}-sirohydrochlorin *a*,*c*-diamide reductase (CfbCD) performs similar reductions for methanogenesis cofactor F430 biosynthesis[11,12] (Fig. 1a). A hallmark of the three isoforms of N_2ase, which are Mo (NifHDK), V (VnfHDGK) and Fe (AnfHDGK) N_2ase, is the presence of two complex metallocofactors, the [8Fe-7S] P-cluster and the active site M-cluster. For Mo and Fe N_2ase, the M-cluster is a [7Fe-9S-C-X-homocitrate] metallocofactor with X = Mo or Fe[13–15] (Fig. 1b). In V N_2ase, the M-cluster is [7Fe-8S-CO_3-C-V-homocitrate] with a carbonate ligand replacing sulfur S3A. M-cluster biosynthesis requires NifB, a radical S-adenosyl-L-methionine enzyme that joins two 4Fe-4S clusters and inserts a central carbide to form the initial [8Fe-9S-C] L-cluster (NifB-co)[13,16]. Further assembly of the FeMo-co and FeV-co requires chaperones NifEN and VnfEN, respectively, whereas FeFe-co assembly occurs in situ[13]. By contrast, regarding the NFL systems for bacteriochlorophyll and F430 biosynthesis, the active site for tetrapyrrole ring reduction is composed of a 4Fe-4S cluster and a hydrophobic substrate binding cavity[9,17,18] (Fig. 1). This comparison suggested that each member of the nitrogenase superfamily has distinct structural features, metallocofactors, substrate specificities and catalytic mechanisms, including the MAR system for reductively cleaving VOSCs.

Here, we present the native isolation and purification of MAR, its catalytic and spectroscopic characterization and an atomic-resolution structure of the oxidized enzyme. Together, they reveal a nitrogenase-like system that utilizes complex metallocofactors matured by MarB or NifB akin to N_2ase for reductive catalysis, and a small binding protein called MarS that regulates activity during unfavourable conditions.

Results

MAR is a two-component system for S acquisition from VOSCs

Initially, we endeavoured to natively purify the MAR system from *Rhodospirillum rubrum*, given that any requisite genes beyond *marB-HDK* were unknown. We grew the organism anaerobically under MAR-inducing conditions (MT-EtOH as the sulfur source)[5] and developed MAR activity assays for VOSC reduction by whole cells and subcellular fractions. MAR enzyme catalysis required ATP, an electron donor, and anoxygenic conditions, analogous to N_2ase and other NFL systems[7,10,11,19] (Table 1 and Extended Data Fig. 1a–c). MAR activity was observed exclusively in the soluble fraction, which was further purified by anion exchange chromatography to 100-fold enrichment in activity. Denaturing gel electrophoresis revealed the presence of multiple protein species (Extended Data Fig. 1b), preventing unambiguous identification of the MAR system and revealing that <0.3 % of total cellular

Table 1 | MAR purification and activity

Sample	Purification step	Total MAR Activity (mU = nmol min^{-1})	Total protein (mg)	Specific MAR activity (nmol min^{-1} g^{-1})	Total cellular protein (%)
R. rubrum native MAR system	Whole cell	12.6	1,600	7.9 ± 2.2	100
	Soluble fraction	12.9	1,332	9.7 ± 2.9	83
	Insoluble fraction	–	–	<1	–
	DEAE eluate	10.2	5.1	2,000 ± 354	0.3
	DEAE flowthrough	–	–	0	–
R. rubrum MAR overproduction system	Whole cell	148	1,760	84 ± 9	100
	Soluble fraction	145	1,440	101 ± 15	82
	Insoluble fraction	–	–	<1	–
	Ni-NTA eluate	575	25	23,000 ± 3,105	1.4
	DEAE eluate	699	20	34,947 ± 4,488	1.1

Activity, enrichment and percentage of total cellular protein by mass of MAR purified natively and from plasmid-based overproduction in *R. rubrum*. Averages and standard deviation error bars are for $n = 3$ independent experiments. DEAE, diethylaminoethanol anion exchange.

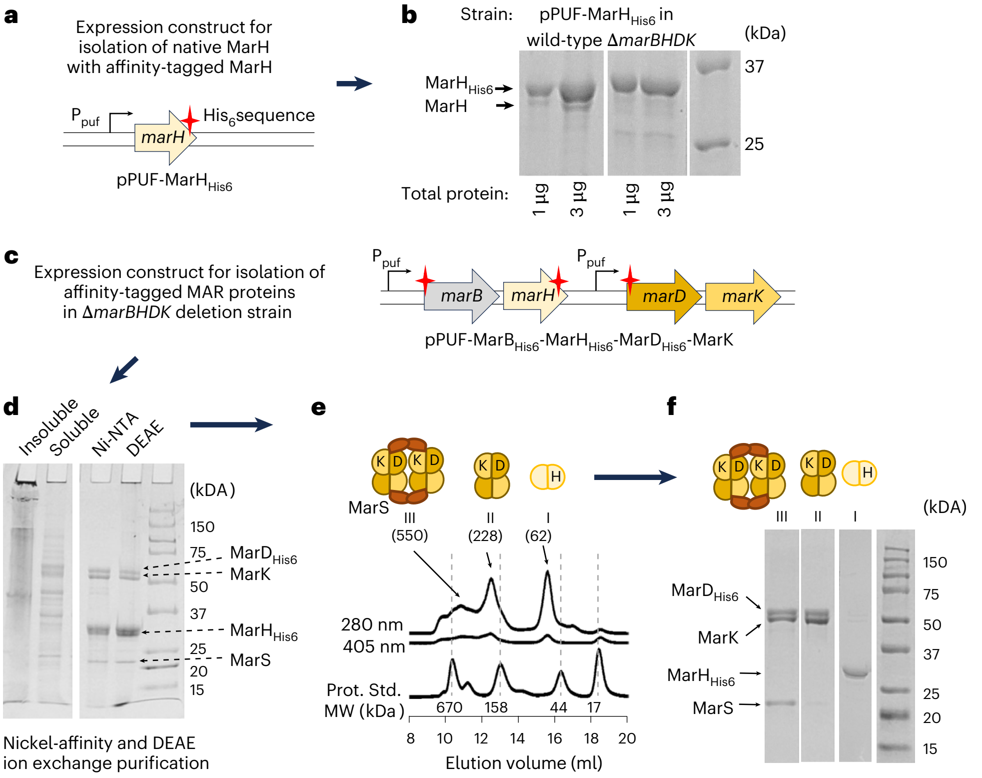

Fig. 2 | Purification and subunit composition of MAR. **a**, Plasmid-based expression system for *marH* gene with poly-histidine sequence (red star) for synthesis of MarH with C-terminal His-tag and pulldown of native MarH. **b**, Abundance of overproduced MarH (using pPUF-MarH$_{His6}$) and natively produced MarH in the wild-type (WT) and *marBHDK* deletion strain. **c**, Plasmid-based expression system for MAR genes with poly-histidine sequences (red stars) for synthesis of MarB N-terminal His-tag, MarH with C-terminal His-tag, MarD with N-terminal His-tag and MarK. **d**, SDS–PAGE of MAR system purification after cell lysis, affinity purification and ion-exchange purification. **e**,**f**, Analytical size-exclusion chromatography of isolated MAR system (**e**) and corresponding SDS–PAGE analysis of subunit composition (**f**). Roman numerals in **e** correspond to the lanes in **f**. Maroon spheres indicate the MarS protein, which interacts with MarDK to form higher molecular weight species and regulate MAR activity. Purification experiments were repeated $n = 2$ times with independent proteins samples with the same results. Prot. Std., protein standard.

protein was composed of MAR. Thus, MAR abundance appears to be ~10-fold lower than when N$_2$ase is induced for N$_2$ fixation (1–10% of total cellular protein)[19].

To overcome this limitation, we constructed a homologous expression system for *marBHDK* in *R. rubrum* such that synthesized MarD possessed an N-terminal six-histidine tag (MarD$_{His6}$) and MarH possessed a C-terminal tag (MarH$_{His6}$), as previously done for N$_2$ase[20,21] (Fig. 2c). MAR genes were expressed under anaerobic conditions in the *R. rubrum marBHDK/nflDK* deletion strain (Δ*marBHDK* Δ*nflDK*). Addition of the histidine-tags did not alter MAR activity in vivo (Extended Data Fig. 1d–f). Through the constructed expression system, total MAR activity increased 10-fold in *R. rubrum*, which again was recovered in the soluble fraction (Table 1). Nickel-affinity purification and anion-exchange polishing further enriched the MAR system by >300-fold to ~99% purity, which corresponded to a MAR abundance of 1% of the total cellular protein (Table 1 and Fig. 2d). The recovered MAR system was

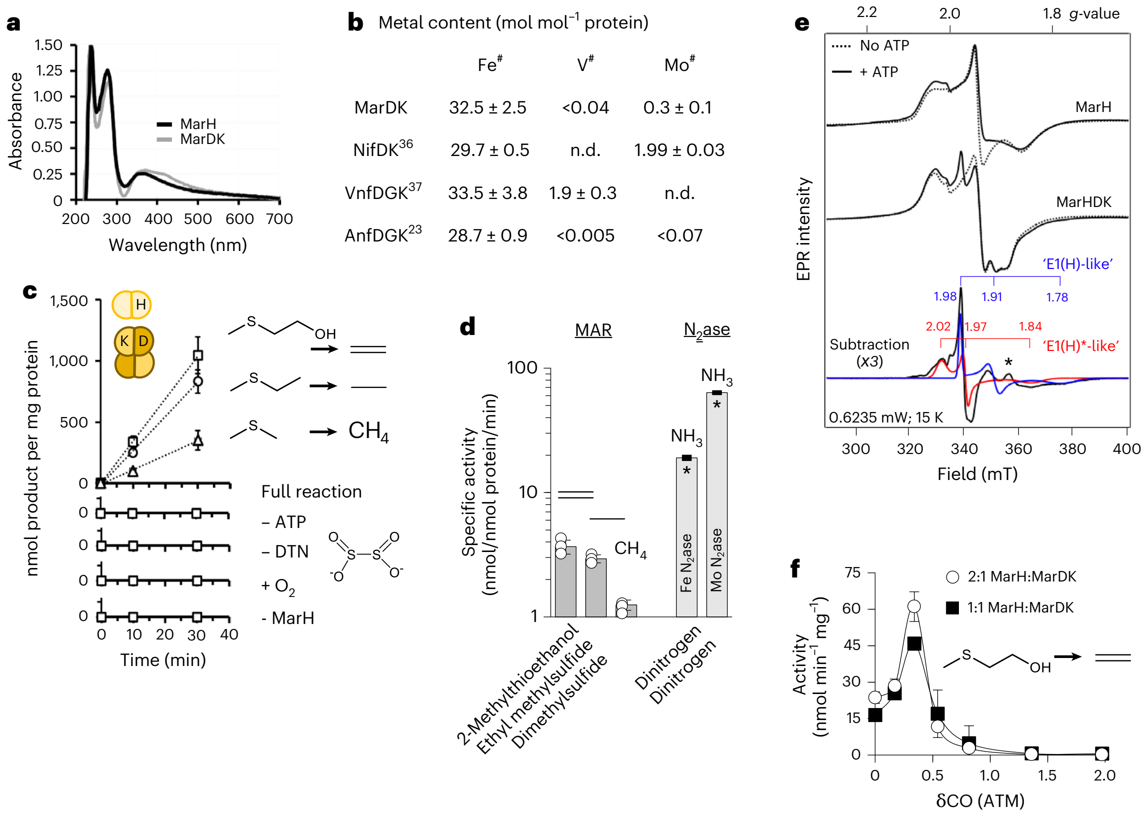

b Metal content (mol mol^{-1} protein)

	Fe$^{\#}$	V$^{\#}$	Mo$^{\#}$
MarDK	32.5 ± 2.5	<0.04	0.3 ± 0.1
NifDK[36]	29.7 ± 0.5	n.d.	1.99 ± 0.03
VnfDGK[37]	33.5 ± 3.8	1.9 ± 0.3	n.d.
AnfDGK[23]	28.7 ± 0.9	<0.005	<0.07

Fig. 3 | MAR activity and metallocofactor characterization. a, UV–vis absorbance spectra of purified MarH and MarDK (Fig. 2f, fractions I and II) under dithionite-reduced conditions. **b**, ICP-MS metal analysis of MarDK compared with Mo, V and Fe N$_2$ase[23,36,37]. The hash symbol indicates the limit of detection in mol mol^{-1} protein: Fe <0.1; V <0.04; Mo <0.004. n.d., not determined. **c**, Functional requirements and activity of purified MarH and MarDK fraction without bound MarS protein (Fig. 2f, fractions I and II) for each known VOSC substrate. MarH = 0.8 µM dimer and MarDK = 0.4 µM tetramer. **d**, Specific activity of MAR with each VOSC substrate obtained by weighted linear regression and standard error calculation from data in **c**, and specific activity of Fe N$_2$ase and Mo N$_2$ase for N$_2$ from Harris et al., 2018 (*)[23]. **e**, CW X-band EPR spectra (ν = 9.38 GHz) of 435 µM MarH dimer ('MarH') and 135 µM MarH dimer + 70 µM MarDK tetramer ('MarHDK') without ATP (dashed) and with ATP (solid). Subtraction of resting-state MarHDK from MarHDK under turnover (shown as *x3* for clarity) with simulated signals results in observed 'E1(H)-like' (blue) and 'E1(H)*-like' (red) species overlaid. The asterisk indicates unidentified residual signal. **f**, MAR activity for MT-EtOH cleavage to ethylene increases, then is inhibited as a function of increasing CO concentrations. Enzyme molar ratios correspond to MarH dimer to MarDK tetramer with MarDK = 0.4 µM. Averages and standard deviation error bars in **b**–**d** and **f** are for $n = 3$ independent experiments. In **c**–**f**, all reactions contained 4 mM ATP, 6 mM dithionite, 1 mM substrate and ATP regeneration system unless otherwise indicated.

composed of a 62 kDa MarH dimer and a 228 kDa MarDK tetramer as resolved by size-exclusion chromatography (Fig. 2e,f, fractions I and II). In addition, an apparent 550 kDa higher molecular weight species was observed to contain *R. rubrum* protein A3441 in complex with MarDK as quantified by proteomics and matrix-assisted laser desorption–time of flight (MALDI-TOF) mass spectrometry (Fig. 2d–f, fraction III; Extended Data Fig. 2). This is consistent with two MarDK tetramers (434 kDa) complexed by two A3441 dimers (88 kDa), and this complex is involved in MAR activity regulation in response to sulfate and light availability (vida infra). The gene for this protein (Rru_A3441) is located at base 3,963,327 on the *R. rubrum* chromosome (NCBI: NC_007643.1) near other genes of unknown function, whereas the *marBHDK* genes are located at base 951,392. We designate the A3441 protein as MarS and corresponding gene *marS* for the MAR switch-off regulator.

MarH possesses a conserved arginine residue, Arg100, which is also found in all N$_2$ases and other NFL systems except COR, and is potentially involved in posttranslational regulation of activity[5]. In *R. rubrum*, Mo N$_2$ase NifH Arg101 is the site of ADP-ribosylation, which prevents NifH binding to NifDK and switches off N$_2$ase activity during periods of darkness and ammonia influx (*R. rubrum* numbering; Arg100 in *A. vinelandii*)[22]. ADP-ribosylation is performed by dinitrogenase reductase ADP-ribosyltransferase (DRAT) and removed by dinitrogenase reductase activating glycohydrolase (DRAG), and their activity is regulated by P-II family regulators. Mass spectrometry analysis of MarHDK proteins showed no posttranslational modifications, and any shifts observed in MarH electrophoretic mobility were due to oxidation or reduction of the peptide (Extended Data Fig. 2a–c). Therefore, the MAR system is not regulated posttranslationally by DRAT and DRAG. This is consistent with the separate roles of MAR and N$_2$ase in sulfur and nitrogen metabolism, respectively.

For reductive C–S bond cleavage of VOSCs by isolated MAR components, MarH alone and MarDK alone exhibited no activity (Fig. 2f, fractions I and II; Fig. 3c). When combined together under the same reaction conditions as before, VOSC cleavage was observed at specific rates of 1–3 nmol substrate per nanomole of protein per minute (Fig. 3c,d). Surprisingly, this is 10-fold lower in specific activity compared with N$_2$ase for N$_2$ reduction[23]. Clearly, in vivo MAR abundance and activity is sufficient for meeting cell sulfur demands, so we quantified MarH abundance through expression of his-tagged MarH as bait for recovery of native MarH (Fig. 2a,b). The overproduced MarH$_{\mathrm{His6}}$ versus native MarH were recovered at abundances of 1% and 0.1% total cell protein, respectively (Fig. 2b and Supplementary Fig. 6; $n = 2$). This confirmed our initial indications that when the MAR system is induced by limiting sulfate conditions, its abundance is 10-fold lower compared with when N$_2$ase is induced by limiting ammonia conditions. For *R. rubrum*, the cellular elemental ratio is $C_1H_{1.7}O_{0.4}N_{0.2}S_{0.002}$, which means that 100-fold less sulfur is needed for cell growth than nitrogen[24]. Therefore, the 10-fold lower specific activity of purified MAR

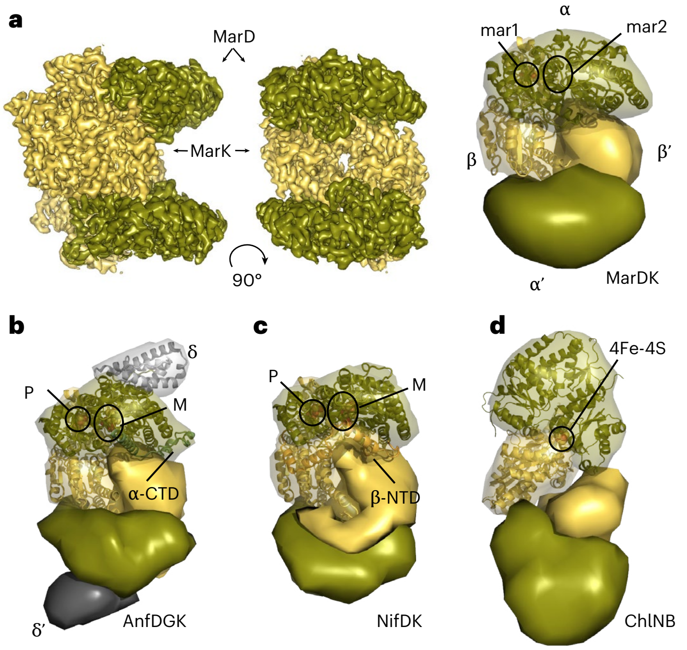

Fig. 4 | MAR cryo-EM structure and nitrogenase superfamily architecture. **a**, Cryo-EM electron density map contoured at 7 sigma and corresponding structural model for MarDK in the oxidized state with locations of MAR metallocofactors (mar1, mar2) indicated (Figs. 5 and 6). **b**–**d**, Structural comparisons of Fe N$_2$ase (Anf; 8OIE)[26] (**b**), Mo N$_2$ase (Nif; 8CRS)[71] (**c**) and DPOR (Chl; 2XDQ)[72] (**d**). Relevant metallocofactors are indicated.

and 10-fold lower abundance of MAR versus N$_2$ase is fully sufficient to fulfil the 100-fold lower sulfur demands, indicating that the observed purified activities are indeed reflective of in vivo activity (Fig. 3c,d). Altogether, this conclusively demonstrates that MarH and MarDK form an oxygen sensitive two-component system that functions in reductive VOSC cleavage in an ATP- and electron-dependent manner (Fig. 1).

MAR structure parallels the nitrogenase fold

Given the successful isolation of MarDK, we sought to determine the structural architecture of MarDK in the absence of MarH (non-turnover conditions) for comparisons with N$_2$ase. Initial attempts in cryogenic electron microscopy (cryo-EM) imaging of the MarDK fraction with MarS were unsuccessful due to population heterogeneity. Therefore, we analysed the MarDK species without MarS by cryo-EM (Fig. 4 and Extended Data Fig. 4). While MAR proteins were purified and handled under anoxic conditions, the final cryo-EM grid blotting was performed under atmospheric conditions (20% O$_2$) due to technical limitations (Methods). However, how oxygen affects MAR is of particular interest, as it is for nitrogenase, because both systems must be properly protected from oxygen for activity in biotechnological applications. On average, the structure was refined to 2.4 Å resolution, and there was a region of no to lower resolution (>3.5 Å) for MarD residues 1–65, 188–197 and 372–409 and MarK residues 1–26 and 88–93 near the surface of MAR, which corresponded to residues predicted to reside underneath and adjacent to where MarH or MarS binds based on AlphaFold 3 models (Extended Data Fig. 5 and 9, Supplementary Fig. 1 and Supplementary Data 1–3). It is currently unknown whether this flexible region is due to lack of MarH or MarS binding, partial denaturation at the air–water interface or protein oxidation during cryo-EM grid deposition. From the cryo-EM structure, it is evident that MarDK is arranged in an $\alpha_2\beta_2$ configuration with C2 symmetry, as seen in all previously characterized N$_2$ase, DPOR and COR systems (Fig. 4). Furthermore, MarD and MarK peptides adopt an architecture similar to the nitrogenase-fold of three subdomains, each composed of four β-sheets (domains I and II) or five β-sheets (domain III) brought into proximity by five α-helices[15,25] (Extended Data Figs. 6 and 7). While the nitrogenase fold is conserved across N$_2$ase, DPOR, COR and MAR systems, there are key differences in the resulting architecture[26,27]. The Mo N$_2$ase has an extended NifK N-terminal domain that pushes up on NifD and skews the DK–D′K′ interface. This is absent in MarDK, VnfDGK and AnfDGK systems, giving MAR an overall architecture that parallels the alternative N$_2$ases (Fig. 4).

MAR metallocofactors resemble N$_2$ase P- and M-clusters

Cryo-EM analysis of MarDK revealed that six cysteine residues are associated with an electron density envelope consistent with a P-like cluster that we designate as the mar1 cluster (Fig. 5a,b). This is in stark contrast to the four coordinating cysteine residues of the 4Fe-4S clusters by DPOR/COR[9,15] (Fig. 4d and Extended Data Figs. 6 and 7). In the fully reduced state (P^N), the P-cluster iron atoms of N$_2$ase are coordinated by six conserved cysteine residues: NifD Cys62, 88, 154 and NifK Cys70, 95, 153 (Fig. 5d; *A. vinelandii* numbering)[15]. AlphaFold 3 models generated for MarDK predict the same six conserved *R. rubrum* MarDK cysteines are positioned to coordinate a P-cluster or P-cluster-like cofactor (Fig. 5c and Supplementary Data 1). These are MarD Cys66, 91, 158, and MarK Cys32, 56, 121, whose *R. rubrum* numbering will be used henceforth[5]. However, in the cryo-EM structure, there are notable differences. MarD Cys66 is not associated with the mar1-cluster electron density, whereas in the AlphaFold 3 model it is positioned to coordinate Fe #7 of a P-cluster (Fig. 5a–c). Rather, in the cryo-EM structure, MarK Cys56 coordinates Fe #7 of the mar1 cluster as compared with coordination of Fe #4 and Fe #5 predicted in the AlphaFold 3 model and equivalent coordination of N$_2$ase P-cluster Fe #4 and Fe #5 by homologous NifK Cys95. However, MarK sequences also possess a seventh cysteine residue, MarK Cys52, which in N$_2$ase is a glycine. MarK Cys52 is observed to coordinate mar1-cluster Fe #4 and Fe #5 in the cryo-EM structure, as compared with the Alphafold 3 model (Fig. 5a–d). Lastly, in the cryo-EM structure, there is a visible ingress in the electron density where Fe #8 of a P-like mar1 cluster would otherwise be expected, such that MarD Cys91 only coordinates Fe #2 as compared with coordination of Fe #2 and Fe #8 in the AlphaFold 3 model and equivalent coordination of N$_2$ase P-cluster Fe #2 and Fe #8 by homologous NifD Cys88. Altogether, the configuration of the six coordinating cysteines in the electron density indicates a P-like cluster in an oxidized state where one of the four central Fe atoms (Fe #8) is missing (Fig. 5a,b). For N$_2$ases, depending on available coordinating residues for oxidation states beyond the catalytically relevant P^{2+} state, one or more of the central Fe atoms is labile to oxidative damage[28,29]. For example, the Mo N$_2$ase NifK residues Ser188 or Tyr98, which coordinate the P^{2+} oxidized state and provide some oxygen protection[28], are absent in MarK[15,30] (*A. vinelandii* numbering; Fig. 5d). Rather, for MarK, these residues are Gly151 and Lys59, respectively. MarK Lys59 is poised to form a salt bridge with MarD Glu68, which in Mo N$_2$ase is also a tyrosine (NifD Tyr64; *A. vinelandii* numbering). The mar1-cluster state in the cryo-EM structure most closely resembles the P-cluster of the previously characterized NifK Ser188Ala mutant, which exhibits reversible Fe loss under oxidizing conditions[29] (Fig. 5e). Thus, the mar1-cluster environment is clearly different from the N$_2$ase P-cluster site for accessing variable coordination across different redox states. Given that the oxidation state of the mar-1 cluster as measured in cryo-EM is currently unknown, we consider that the MarD Cys52 and Cys56 may be involved in coordinating the mar-1 cluster in other redox states throughout the catalytic cycle[31].

For catalysis the N$_2$ase M-cluster is coordinated by a conserved cysteine and histidine residue: NifD Cys275 and His442 (Figs. 4c and 6c; *A. vinelandii* numbering)[15,25]. Coordinately, previous sequence alignment suggested that the conserved MarD Cys270 and nearby His450 could serve as ligands for a MAR catalytic metallocofactor[5]. In the cryo-EM density map, there was no indication of a

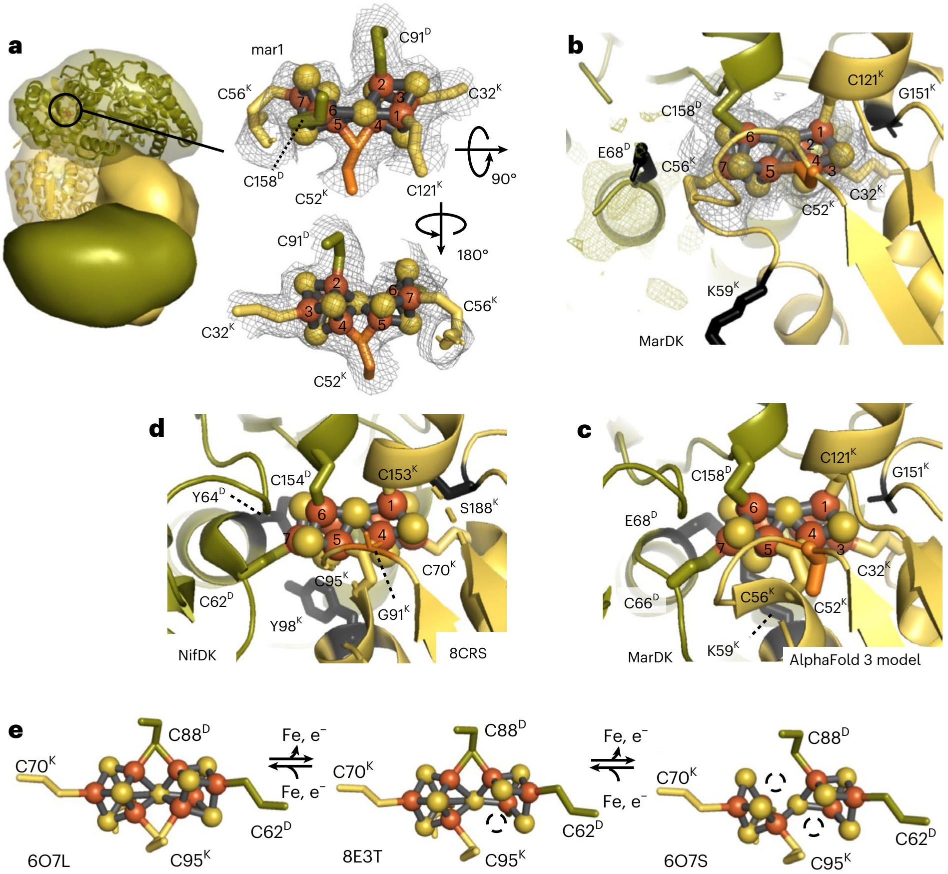

Fig. 5 | MarDK mar1 cluster and N_2ase P-cluster coordination. a, Cryo-EM electron density contoured at 5 sigma with 2 Å buffer around the mar1 cluster and coordinating cysteine residues. **b**, Same electron density contour as in (**a**), also showing the local MarDK protein environment. The electron density for the mar1 cluster indicates an oxidized P-like cluster with missing Fe #4. **c**, AlphaFold 3 model of MarDK in the mar1-cluster region, showing that the six cysteines conserved with N_2ase are predicted to be positioned to coordinate a metallocofactor consistent with a reduced P-cluster (P^N shown) as in N_2ase. **d**, Structure of *A. vinelandii* NifDK (8CRS)[71] in the P-cluster region showing P^N coordination by the six conserved cysteines. In N_2ase NifK Gly91 replaces MarK Cy52 (orange). **e**, Progressive oxidation of labile P-cluster irons of *A. vinelandii* NifK S188A, which is analogous to the MarK G151 residue of MAR[28,29]. Superscript D indicates the MarD or NifD subunit and superscript K indicates the MarK or NifK subunit.

metallocofactor in this region. This is consistent with the presumed catalytic metallocofactor being oxidatively damaged during deposition for cryo-EM. Interestingly, we observed a second histidine in this region that is not found in NifD, MarH His429, which is located on the loop after helix 18 (Fig. 6a–c). MarD His429 is in closer proximity to MarD Cys270 than MarD His450, which is located on the loop before helix 19 (9.6 Å versus 10.5 Å). Indeed, when we substituted MarD Cys270 with Ala or MarD His429 with Phe or Leu, this resulted in a completely inactive enzyme, analogous to when the Mo N_2ase M-cluster ligands NifD Cys275 and NifD His442 are mutated[32] (Fig. 6d). Substitution of MarD His450 and the only other cysteine residue in the region, MarD Cys73, had no effect. Collectively, these results suggest that MarD His429 and MarD Cys270 coordinate a metallocofactor, which is supported by AlphaFold 3 modelling showing an L-cluster coordinated between these residues (Fig. 6c and Supplementary Data 1).

Coordination of an active site metallocofactor in the region of MarD His423 and Cys270 is further supported by mutational analysis of MarD α-helix 9. In Mo N_2ase, NifD α-helix 9 contains Gln191 and His195 for coordinating the substrate and M-cluster labile sulfur S2B above the M-cluster active site[7,15,33] (Fig. 6c; *A. vinelandii* numbering). In MarD, these are replaced by hydrophobic Trp195 and Phe199 residues, respectively, with adjacent His194 and Asp200 (Fig. 6a,b; *R. rubrum* numbering)[5]. MarD Trp195 was required for catalysis (Fig. 6d), providing initial evidence that this residue may be involved in structuring the protein environment around the active site metallocofactor for cleavage of hydrophobic VOSCs.

Consistent with MarDK possessing multiple complex metallocofactors, it exhibits a broad multifeatured ultraviolet–visible (UV–vis) absorption spectrum near 400 nm as seen for N_2ase[34,35] (Fig. 3a). Inductively coupled plasma mass spectrometry (ICP-MS) metal analysis of MarDK reveals a metal content of ~32 Fe per MarDK tetramer and negligible vanadium or molybdenum (Fig. 3b). The iron content is similar to the 30–32 Fe found in N_2ase from the P- and M-cluster (Fig. 1a), and parallels Fe N_2ase, which contains only Fe[23,36,37]. This is in stark contrast to DPOR and COR, which contain only 8 Fe per tetramer due to one 4Fe-4S cluster at each heterodimer interface[9]. To further probe the MAR metallocofactors, we performed electron paramagnetic resonance (EPR) spectroscopy on MarH and the MarHDK complex under turnover and non-turnover conditions. The continuous-wave (CW) X-band EPR spectrum of isolated MarH in the absence of ATP exhibits signals consistent with a spin state (S) mixture of $S = ½$ species (g-tensor values: $g_1, g_2, g_3 = [2.03, 1.93, 1.85]$; $g_{iso} = 1.94$) and $S = 3/2$ species ($E/D = 0.21$; $D < 0$; where E/D is the rhombicity of the zero field splitting tensor and D is the zero field splitting tensor) in a 1:5 ratio. In the presence of ATP, the EPR lineshapes of the $S = ½$ and $S = 3/2$ signals change (Fig. 3e and Extended Data Fig. 3b–d), similar to observations in the EPR spectra of the $[4Fe\text{-}4S]^+$ cluster of NifH, VnfH and AnfH[38–40]. This observed behaviour suggests that, analogous to the iron proteins of nitrogenase[40], MarH undergoes a conformational change upon binding of ATP. The EPR spectrum of MarHDK in the absence of ATP exhibits an attenuated $S = 3/2$ signal relative to MarH alone and an intense, near-axial signal around $g = 2$, characteristic of a $[4Fe\text{-}4S]^+$ cluster, which we attribute

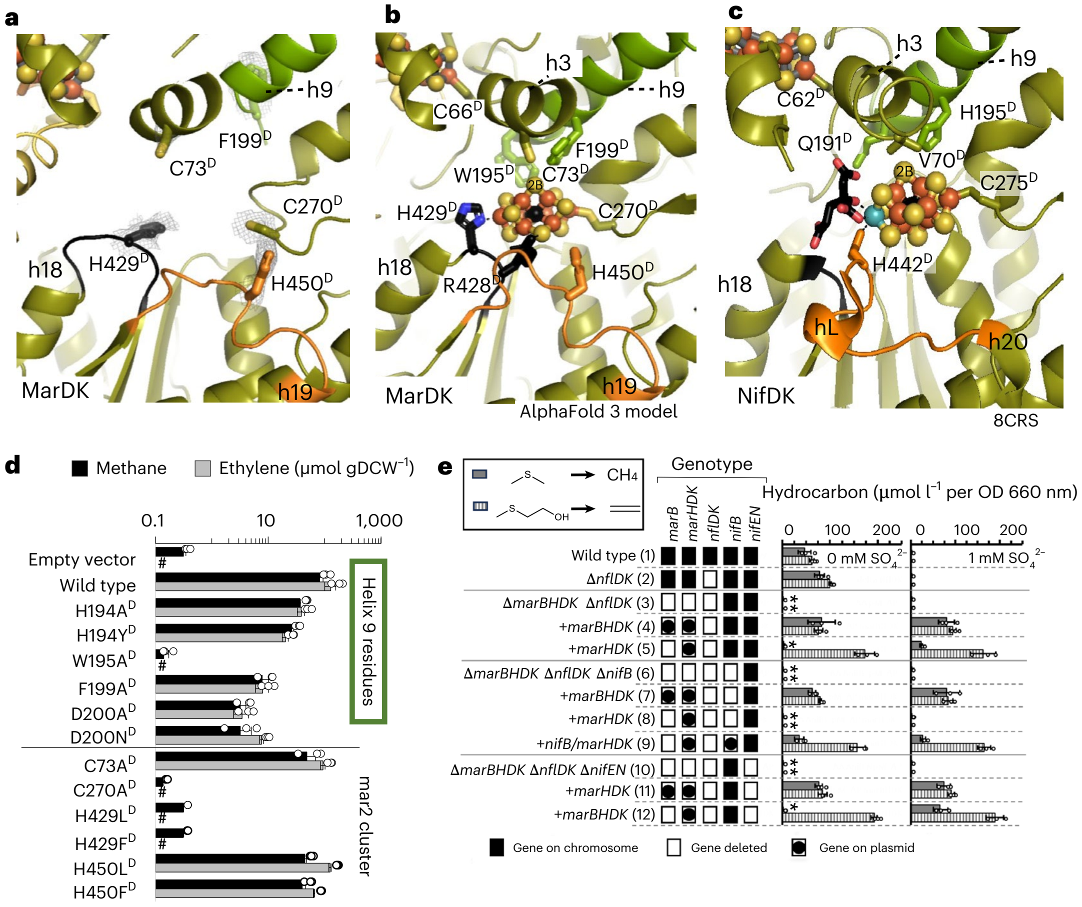

Fig. 6 | MarDK mar2-cluster region and MAR metallocofactor maturation by MarB and NifB. a,**b**, Cryo-EM of oxidized MarDK (**a**) and AlphaFold 3 model of MarDK (**b**) in the proposed mar2-cluster region. **c**, The structure of NifDK (8CRS)[71] showing coordination of FeMo-co. The loop before helix 18 (black) contains MarD His429 required for MAR catalytic activity, which is absent in NifD. For NifD, the loop before helix 20 (orange) contains the M-cluster coordinating His442 along with left-handed helix hL. NifD and MarD helix h9 shown in green. **d**, In vivo MAR cleavage of VOSCs for site-specific amino acid substitutions of MarD. The hash symbol indicates a value below detection limit of 0.05 µmol. gDCW, grams dry cell weight. **e**, In vivo MAR cleavage of VOSCs when *marBHDK*, *nflDK*, *nifB* and *nifEN* genes are present on the chromosome, deleted or restored in trans from a plasmid. NifB or MarB is required for activity but not NifEN. MAR genes on the chromosome are regulated by SalR and expression is repressed by 1 mM sulfate[5]. When *mar* and *nif* genes are on the plasmid, they are constitutively expressed. OD, optical density. The asterisk indicates strains could not grow on DMS or MT-EtOH as the sole S source. All other strains grew to a final optical density of 2.0 in 48 h. Averages and standard deviation error bars in **d** and **e** are for $n = 3$ independent experiments. Superscript D indicates the MarD or NifD subunit and superscript K indicates the MarK or NifK subunit.

primarily to MarH[36–38] (Figs. 1a and 3e and Extended Data Fig. 3c). In the presence of ATP, several new features are observed spanning from $g = 2.02$ to 1.77. Subtraction of the resting-state spectrum reveals two major rhombic species with $g_1, g_2, g_3 = [1.98, 1.91, 1.78]$ ($g_{iso} = 1.89$) and $g_1, g_2, g_3 = [2.02, 1.97, 1.84]$ ($g_{iso} = 1.94$) in an approximately 1:1 ratio (Fig. 3e and Extended Data Fig. 3a). These features closely resemble those of the Fe N$_2$ase E1(H) species ($g_1, g_2, g_3 = [1.965, 1.928, 1.779]$; $g_{iso} = 1.89$) and E1(H)* species ($g_1, g_2, g_3 = [2.009, 1.950, 1.860]$; $g_{iso} = 1.94$), which are catalytic intermediates observed under analogous turnover conditions. These signals are not expected to arise from canonical FeS clusters[36,39]. Spin quantitation of the EPR signal of MarHDK with and without ATP indicates the signals derive from active holo-enzyme (Extended Data Fig. 3d). Consistent with the elemental analysis that shows the presence of only iron, there are no EPR signals indicative of a FeMo-co or FeV-co at low fields in samples of MarHDK[15,29,37,41,42] (Extended Data Fig. 3b,c). Taken together, these results are consistent with a second metallocofactor at the active site of MarDK that resembles FeFe-co bound to MarD Cys270 and His429, which we designate the mar2 cluster.

Lastly, similarity between mar2 and FeFe-co is further supported by considering the CO inhibition profile for MT-EtOH reduction to ethylene by MAR. As δCO was increased from 0 to 0.4 atm, MAR activity for MT-EtOH reduction to ethylene concomitantly increased above baseline. However, at δCO > 0.4 atm, the observed activity decreased until ultimately rendering the enzyme inactive (Fig. 3f and Extended Data Fig. 2f). This behaviour resembles that observed for acetylene reduction by the V N$_2$ase. While the Mo N$_2$ases show a strict inhibition by CO for a 2e$^-$ reduction of acetylene to ethylene at δCO ≤ 0.001 atm (ref. 43), the 2e$^-$ reduction of acetylene to ethylene by V N$_2$ase displays a similar initial activity enhancement in the presence of CO under low electron flux conditions, followed by a decrease when δCO > 0.1 atm. The presence of CO also enhances the 4e$^-$ reduction of acetylene to ethane, up to 0.1 atm. This biphasic behaviour is attributed to the two separate binding sites for CO on the M-cluster[43,44]. The similarity in CO enhancement and inhibition profiles between MarDK and VnfDK provides initial evidence that MarDK interacts with CO during VOSC reduction in a similar manner as nitrogenases.

MAR maturation utilizes MarB or N$_2$ase NifB

A striking feature of MAR gene clusters in bacteria is the presence of a highly conserved *nifB* homologue we designated *marB*[5]. MarB sequences contain the same conserved domains that NifB utilizes

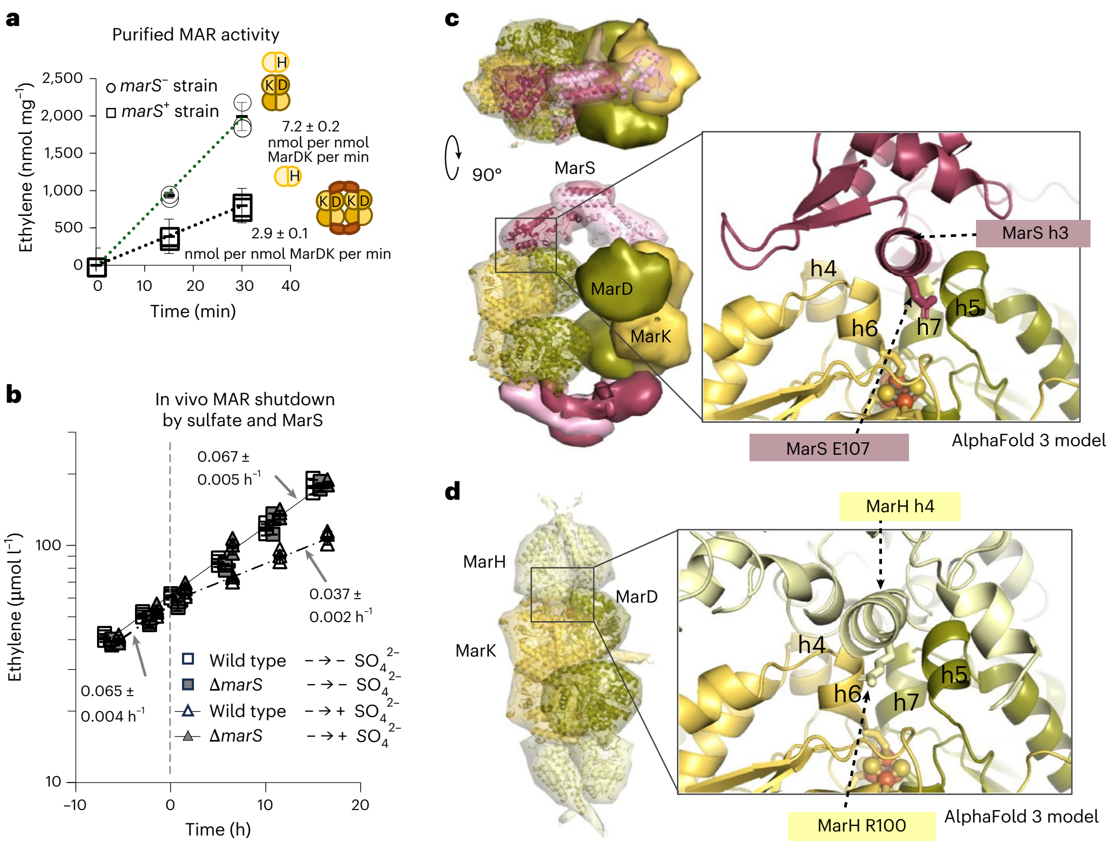

Fig. 7 | MarS is involved in MAR activity switch-off upon sulfate influx. **a**, Activity of MarHDK isolated from a *marS* deletion strain (*marS*⁻, strain Δ*nflDK* Δ*marBHDK* Δ*marS*,) compared with activity of MarHDK with MarS isolated from the *marS* competent strain (*marS*⁺, strain Δ*nflDK* Δ*marBHDK*). MarH = 0.8 µM dimer and MarDK = 0.4 µM tetramer. **b**, In vivo MAR activity change upon influx of sulfate at time *t* = 0 in a *marS*⁺ (wild-type) and *marS*⁻ strain (Δ*marS*) initially grown on MT-EtOH as the sole sulfur source for maximum initial MAR activity. Lines are exponential fits to ethylene production by strains before and after sulfate addition showing a 2-fold change in ethylene rate constant. As the cultures grow exponentially, ethylene production follows the same exponential trend. In **a** and **b**, averages and error bar standard deviations are for *n* = 3 independent experiments. **c**,**d**, Representative AlphaFold 3 models of MarS and MarH binding to MarDK (Supplementary Fig. 1 and Supplementary Data 1–3).

for synthesis of the [8Fe-9S-C] NifB-co (L-cluster) precursor of the M-cluster[5] (Fig. 1b). Using a genetic approach, we characterized the role of MarB in MAR maturation. First, we verified that no Nif, DPOR or COR components of *R. rubrum* could replace MarH or MarDK, given previous reports of cross-interaction between nitrogenase superfamily components[45] (Extended Data Fig. 8). This allowed us to test the requirement of MarB for MarHDK activity, which resulted in two key observations. First, in the absence of MarB, MAR activity was still present, and second, in vivo cleavage of DMS to methane decreased while MT-EtOH cleavage to ethylene increased (Fig. 6e, strains 1–5). Given the high (48%) sequence similarity between MarB and NifB[5], we questioned whether NifB could function in lieu of MarB. Indeed, when NifB and MarB were both absent, no MAR activity was possible. Then, when NifB was restored in trans from a plasmid, the same differential production of methane versus ethylene was observed as when NifB was the sole maturase present on the chromosome (Fig. 6e, strains 5–9). This demonstrates that MarB and NifB individually can mature MarDK into a functional system and further establishes that M-like clusters function in systems beyond N_2ase. Moreover, as with the Fe N_2ase, activity does not require chaperone NifEN, indicating MarB and NifB directly interact with MarDK for metallocofactor assembly[13] (Fig. 6e, strains 10–12).

MarS represses MAR activity upon sulfate influx or darkness

Based on sequence identity, MarS belongs to the phenolic acid decarboxylase regulator (PadR) winged helix family of proteins and shares 32% identity with the canonical PadR regulator from *Bacillus subtilis*[46]. The AlphaFold predicted structure (UniProt: Q2RNRO) contains a C-terminal dimerization domain, a winged-helix domain and a low-complexity N-terminal region that is 30% of the total peptide length (Extended Data Fig. 2d,e). MarS is not a sequence homologue of the V or Fe N_2ase G-subunit, CowN protein for CO protection, or the Shethna protein II (FeSII) for O_2 protection[47–51]. Therefore, we took an in vivo approach to determine MarS function by measuring growth and MAR activity in the wild-type (*marS*⁺) and MarS deletion strain (*marS*⁻). In the presence of oxygen, MarS did not confer any oxygen protection for growth using VOSCs (Extended Data Fig. 10c). Also, MarS was not required for CO protection, as no growth inhibition was observed in the presence of 0–0.1 atm CO. This is consistent with the observation that purified MAR is inhibited only above δCO >0.4 atm (Fig. 3f and Extended Data Fig. 10d). Instead, MarS is observed to function in switching-off MAR activity during sulfate influx, or darkness when ATP cannot be efficiently made by photophosphorylation. This is proposed to prevent unnecessary use of ATP akin to N_2ase switch-off by DRAT during ammonium influx and darkness[22] (Fig. 7b and Extended Data Fig. 10b). Coordinately, we simultaneously grew and purified MAR from *marS*⁺ and *marS*⁻ strains to eliminate any effects of MarS on MAR activity. MarHDK isolated from the *marS*⁻ strain exhibited 2-fold more activity than MarHDK isolated with MarS under standard reaction conditions, consistent with in vivo results (Fig. 7a). Both the decrease in MAR activity and coordination of two MarDK tetramers into a larger structure by MarS is corroborated by AlphaFold 3 models of MarS, PadR or MarH binding to MarDK (Extended Data Fig. 9 and Supplementary Fig. 1). In all models of MarS and MarDK multimerization, four MarS monomers formed two dimers that bridged two adjacent MarDK tetramers (Fig. 7c and Supplementary Fig. 1). Notably, MarS helix 3 is predicted to insert adjacent to MarD helix 5 and MarK helix 6 in a similar fashion to MarH helix 4. This is analogous to but distinct from Mo N_2ase regulation by DRAG and DRAT. For NifH, conserved helix 4 interacts with NifD helix 5 and NifK helix 9 (Extended Data Figs. 6 and 7) and contains NifH Arg101 that is required for catalysis (*R. rubrum* numbering; Arg100 in *A. vinelandii*)[52]. NifH Arg101 ADP-ribosylation by DRAT disrupts the NifH–NifDK interaction interface to inhibit N_2ase activity, whereas with MarH there is no evidence for MarH Arg100 ADP-ribosylation (Extended Data Fig. 2). Altogether, this points to a mechanism where MarS regulates MAR activity by binding and multimerizing MarDK to block key MarH interactions with MarDK. Currently, what triggers MarS binding and release for MarDK multimerization is unknown, but there is precedence for multimerization of nitrogenase. In *Azotobacter vinelandii,* the Shethna FeSII protein, upon oxidation of the FeS cluster, inserts between NifDK and NifH to turn off Mo N_2ase and protect the metallocofactors from oxygen damage. This serves as a nucleation site for the association of additional FeSII, NifDK and NifH components into larger filamentous complexes thought to provide additional sequestration of N_2ase from oxygen[50,51]. The binding of MAR to MarS is clearly different, as no MarH is associated in these complexes. Thus, it appears that nature has evolved mechanisms to regulate MAR activity in response to sulfate and energy availability by inhibiting MarH binding in a mechanism distinct from how nitrogenase activity is regulated by DRAT or FeSII in response to ammonia or oxygen, respectively.

Discussion

The nitrogenase superfamily has evolved enzyme systems not only for nitrogen fixation (N_2ase) and carbon/energy metabolism (DPOR, COR and CfbCD), but also for sulfur metabolism (MAR) based on the nitrogenase-fold domain (Fig. 4 and Extended Data Figs. 6 and 7). MarHDK is the catalytic system that produces methane from DMS and ethylene from MT-EtOH in *R. rubrum* and other organisms with MAR homologues[5]. This explains how ethylene would be made from MT-EtOH by organisms with MAR in anoxic soils[3] and represents a promising alternative route for microbial production of this platform chemical to reduce reliance on fossil fuels.

The regulation of MAR activity through the binding and dissociation of the PadR family protein MarS is thought to be mediated by allosteric mechanisms. The canonical PadR regulator binds phenolic acid family molecules in an interdomain pocket between helix 6 and helix 5′ via residues Arg164, Lys127, His154 and Thr93′. Effector molecule binding allosterically induces PadR to dissociate from the DNA through an interdomain-reorganization mechanism[46]. While these effector molecule coordination residues are not conserved in MarS, we anticipate that specific residues in the analogous MarS helix6 and helix 5′ region, or the glycine-rich N-terminal tail (not present in PadR), will be involved in binding of effector molecules, albeit currently unknown, that are associated with the presence or absence of sulfate and light. Such binding would presumably result in MarS conformational changes that trigger association or dissociation from MarDK.

Strikingly, beyond MAR, the vast majority of group-IV NFL gene clusters that continue to be of unknown function also contain a conserved *marB*/*nifB* homologue. Coordinately, the NFL homologues of NifDK contain the same conserved cysteines used by N_2ase for P-cluster coordination and conserved NifD Cys275 residue used by Mo N_2ase for M-cluster coordination[5]. The observation that both MarB and NifB can mature the presumed MarDK mar2 cluster—and that this activity requires the conserved MarD residues Cys270 and the novel His429—strongly suggests something similar to the nitrogenase [8Fe-9S-C] L-cluster (NifB-co; Fig. 1b) is at the core of the catalytic metallocofactors throughout NFL systems of unknown function. Given the differential activities of the MAR system towards DMS versus MT-EtOH when assembled with MarB versus NifB, the bona fide mar2 cluster made by MarB is suggested to be distinct from the cofactor made by NifB. Alternatively, it may be the same cofactor but placed in a different orientation by the two maturases, resulting in an altered coordination environment that affects substrate binding and/or formation of catalytic intermediates. The observed EPR signal similarities of MarH to NifH, VnfH and AnfH and the similarities of MarHDK to the E1(H) and E1(H)* intermediates of Fe N_2ase provide the first spectroscopic evidence that the mar2 cluster resembles FeFe-co[41,53]. Moreover, in Fe N_2ase, these two species are postulated to interconvert via displacement of a bridging hydride within the M-cluster. This suggests that, like nitrogenase, the catalytic cofactor accumulates reducing equivalents in the form of hydrides and, thus, may be activated via sulfur release before reacting with substrate[53]. So far, the complex nitrogenase M-clusters and their L-cluster precursors have been unprecedented outside of nitrogenase enzymes. This has been attributed to specific evolution required to overcome the extreme stability of the N≡N bond[7,33]. The discovery of metallocofactors in MAR resembling the nitrogenase P- and M-clusters suggests that these catalysts evolved not only for nitrogen reduction, but also for sulfur reduction—and probably for broader roles in transforming essential elements into biologically accessible forms.

Methods

Chemicals and helper enzymes

All chemicals were of reagent purity or higher and were obtained from Sigma-Aldrich, except for ethylmethyl sulfide and (2-methylthio) ethanol, which were from ThermoFisher. Creatine phosphokinase was from Sigma-Aldrich. All restriction enzymes and T4 ligase were from New England Biolabs (NEB), and Phusion DNA Polymerase was from ThermoFisher.

Bacterial strains and growth conditions

All *Rhodospirillum rubrum* strains used in this study are derived from wild-type strain S1 (ATCC 25922)[54] as follows:

Strain	Genotype	Reference
Δ*nflDK*	Δ0772:3; St^R	5
Δ*nflDK* Δ*marBHDK*	Δ0772:3 Δ0793:6; St^R	5
Δ*nflDK* Δ*marBHDK* Δ*nifB*	Δ0772:3 Δ0793:6 Δ0994; St^R	This work
Δ*nflDK* Δ*marBHDK* Δ*nifEN*	Δ0772:3 Δ0793:6 Δ2285:6; St^R	This work
Δ*marS*	Δ3441; St^R, Gm^R	This work
Δ*nflDK* Δ*marBHDK* Δ*marS*	Δ0772:3 Δ0793:6 Δ3441; St^R, Gm^R	This work
Δ*nflDK* Δ*marBHDK* Δ*nifB* Δ*marS*	Δ0772:3 Δ0793:6 Δ2285:6 Δ3441; St^R, Gm^R	This work

Strains were grown in Ormerod's sulfur-free malate minimal medium supplemented with 1 mM $(NH_4)_2SO_4$ and/or 1 mM VOSC under anaerobic conditions with 95% N_2:5% H_2 gaseous headspace with appropriate antibiotics (50 µg ml^{-1} streptomycin, 25 µg ml^{-1} kanamycin and 1–4 µg ml^{-1} tetracycline)[5,55]. Ormerod's medium was made sulfur free by replacing all sulfate-complexed metals with chloride versions. All in vivo growth and activity analyses were performed in 10 ml medium in anaerobic stoppered test tubes. All growth for protein purification and characterization was performed in 1- and 2-l Roux bottles. All strains were grown at 30 °C under 2,000 lux for growth experiments and 3,000 lux for protein production. All strain manipulations were performed in a Coy anaerobic chamber with 95% N_2:5% H_2 atmosphere. Cell growth for quantification of hydrocarbons produced from VOSCs by wild-type and modified MAR enzyme systems, cell growth for CO and O_2 inhibition of MAR activity in vivo and cell growth for measuring sulfate influx and dark switch-off of MAR activity in vivo are fully detailed in the Supplementary Methods.

Plasmid construction for gene deletions and substitutions

Plasmids, primers and restriction enzyme sites for plasmid construction of truncated gene fragments for gene deletions listed in the 'Bacterial strains and growth conditions' section, construction of *marBHDK* and *nifB* complementation plasmids, and construction of plasmids with *marDK* mutations corresponding to site-specific amino acid substitutions are provided in Supplementary Tables 2 and 3. All constructed plasmids and chromosomal gene deletions were verified by Sanger sequencing.

Gene deletions

gene deletions were performed in the wild-type and Δ793:6Δ772:3 strains using homologous recombination methods established for *R. rubrum*[3,5]. In brief, all deletions were in-frame deletions except for deletion of the A3441 gene, which was a deletion and insertion of a gentamycin antibiotic resistance cassette. For each gene, 1,000 nucleotides (nt) upstream and the first 10–15 codons were amplified by PCR using primers to include a 5′ restriction site and a 3′ XbaI site. Similarly, the last 10–15 codons and 1,000 nt downstream were amplified by PCR using primers to include a 5′ SpeI site and a 3′ restriction site. PCR products were first digested and ligated together using the XbaI/SpeI sites to generate the truncated fragment, which was then digested and ligated into correspondingly digested pK18MobSacB. Plasmids were transferred to *Escherichia coli* stellar cells (TaKaRa) and then to *R. rubrum* by triparental mating with *E. coli* JM109:pRK2013 (ATCC 37159). First-recombination events were screened based on presence of sucrose sensitivity and kanamycin resistance (Km^{R}) from integration of the pK18mobsacB plasmid. Second-recombination events were screened based on loss of sucrose sensitivity and Km^{R}.

Gene complementation of *marBHDK* and *nifB*

All complementation studies utilized pBBR1-MCS3 based plasmid[56], pMTAP-MCS3, which contains the *R. rubrum* constitutive MTA phosphorylase promoter and tetracycline resistance gene (Tc^{R}) exactly as previously used for *marBHDK* gene complementation in *R. rubrum*[3,5]. For each gene combination, the first gene was amplified by primers to contain an NdeI site at the ATG start codon, which correctly positioned the start codon relative to the MTA phosphorylase promoter ribosome binding site. All other genes utilized their associated ribosome binding site. All genes were amplified by PCR from the *R. rubrum* genome using primers and cloned into pMTAP-MCS3 using restriction sites listed in Supplementary Tables 2 and 3.

Mutagenesis and complementation of *marBHDK* genes

Plasmid pMTAP with the *marBHDK* genes is too large for amplification by PCR to directly incorporate nucleotide substitutions for site-directed mutagenesis. Therefore, *marDK* was digested from pMTAP-MarBHDK by KpnI and XbaI and cloned into the same sites of pUC19 (Invitrogen). Site-directed mutagenesis was performed by the Quick-Change Lightning kit (Agilent) using complementary primers. Modified *marDK* genes were then digested from pUC19 by KpnI and XbaI cloned into pMTAP-MarBHDK to replace the original *marDK* sequence.

Gas chromatography analysis of hydrocarbons

Quantification of methane, ethane and ethylene was performed using a Shimazdu GC-14A with Restek Rt-Alumina BOND/Na2SO4 column, 30 m, 0.53 mm inner diameter. Gaseous culture headspace after feeding or growth experiments was injected at 180 °C and separated isothermally at 35 °C. Eluted compounds were detected by flame ionization detector at 180 °C and identified on the basis of the retention time of methane, ethane and ethylene standard (Schott; Air Liquide). The total amount of each hydrocarbon present was calculated from the peak area as compared with standard concentration curves of the corresponding reference standard.

Overexpression plasmid for marBHDK for purification

Expression plasmids were based on *R. rubrum* complementation plasmid pMTAP[3,5]. The promoter of pMTAP-MCS3 was replaced with the *R. rubrum* PUF promoter. This promoter for the light harvesting complex genes *pufLMB*, which are next to the COR *bchXYZ* operon, is a strong promoter under anaerobic conditions[57]. The PUF promoter and *marBHDK* genes were cloned into pMTAP-MCS3 as described in the Supplementary Methods. This resulted in the following plasmids:

- pPUF-MCS3
- pPUF-M4 (pPUF plasmid with PUF promoter, *marBH*, PUF promoter, and *marDK*)
- pPUF-MarB$_{\text{His6}}$-MarH$_{\text{His6}}$-MarD$_{\text{His6}}$-NifK (same as pPUF-M4 but with His6-tag sequences)
- pPUF-MarH$_{\text{His6}}$

Purification of MAR

All MAR proteins produced in *R. rubrum* were resolved by sodium dodecyl sulfate–polyacrylamide gel electrophoresis (SDS–PAGE) electrophoresis using 12% acrylamide gels (Bio-Rad), and all original gel images with cropped areas indicated are given in Supplementary Figs. 2–5.

All purification steps were performed in a Coy anaerobic chamber. Purification followed the standard published procedures for *A. vinelandii* nitrogenase with important aspects and differences detailed in the Supplementary Methods[58]. Purified protein samples were frozen by adding dropwise to liquid nitrogen and storing the resulting beads at −80 °C in anaerobic serum vials.

ICP-MS, MALDI-TOF and proteomic analysis

Rhodospirillum rubrum MarDK with MarS (A3441 protein) was resolved by SDS–PAGE, washed extensively in ultrapure water, stained with Coomassie-G stain in 40 % methanol/10 % acetic acid, destained with 40 % methanol/10 % acetic acid and washed extensively with water. The A3441 protein band was excised and analysed by in-gel trypsin digestions followed by extraction and liquid chromatography–tandem mass spectrometry quantitation by the Ohio State University Campus Chemical Instrument Center following standard protocols[59]. Protein A3441 was the only *R. rubrum* protein identified in high abundance; all other proteins of notable abundance were human keratin. MALDI-TOF of purified MarHDK and MarS proteins was performed on a Bruker Microflex LRF with sinapic acid matrix. All MADLI-TOF was performed on at least $n = 2$ independent sample preparations (Supplementary Fig. 2). ICP-MS of metal content was performed at the University of Georgia Center for Applied Isotope Studies. Purified MarDK + MarS was desalted by centrifugal concentration at 4 °C in 25 mM Tris pH 7.5, 50 mM NaCl treated with CHELEX resin to remove trace metals. Proteins and buffer control were digested by nitric acid and analysed by ICP-MS based on standard curves for Mg, Fe, V, Mo, Co, Cu and Ni. Analysis was performed on protein from $n = 3$ independent sample preparations.

MAR activity and CO inhibition assays

Activity assays in cell extracts, partially purified fractions and fully purified preparations were performed similarly to the standard purified N$_2$ase activity assay. All experiments were performed anaerobically on a Schlenk line. Reactions of 500 µl volume were performed in 2-ml serum vials with 500 mg total cellular or soluble/insoluble protein fractions, or 13–25 µg MarH and 50 µg MarDK (with or without MarS protein) for a 1:1 or 2:1 MarH dimer to MarDK tetramer molar ratio. Reaction conditions contained 100 mM HEPES pH 7.5, 6 mM dithionite, 5 mM MgCl$_2$, 1 mM substrate and ATP regeneration system (20 mM creatine phosphate and 0.1 mg ml^{-1} creatine phosphokinase). Reactions were initiated by addition of ATP by gas-tight syringe, incubated at 30 °C under nitrogen atmosphere for 5–60 min and quenched with 1/10th volume 100% trichloroacetic acid. For CO inhibition assay, the procedure was performed in the same manner, but CO was added to the nitrogen headspace at the indicated partial pressure and incubated for 1 min before initiating the reaction with addition of ATP. Protein concentration in cellular protein extracts and soluble/insoluble fractions were quantified by Bradford assay with BSA as a standard.

EPR spectroscopy

Samples under turnover and non-turnover conditions for EPR were prepared as above for activity assays with the following alterations. MarDK+A3441 as added to 21.4 mg ml^{-1} (70 μM) and MarH to 8.6 mg ml^{-1} (135 μM) in a 175-μl reaction volume containing the same buffer and ATP regeneration system as above plus 20% glycerol as a glassing agent. This corresponded to a 1:2 ratio of MarDK tetramer to MarH dimer. Similarly, MarH alone in the same conditions was added to 28 mg ml^{-1} (435 μM). At time $t = 0$, no ATP or ATP to 4 mM concentration was added, rapidly mixed and immediately transferred to a quartz EPR tube. After 30 s incubation time at room temperature, samples were frozen in liquid-nitrogen-cooled isopentane. CW X-band (9.376 GHz) EPR spectra were collected using a Bruker EMXPlus equipped with an ColdEdge cryogen-free helium cryostat and recirculation system and an Oxford Instruments MercuryITC temperature controller at both 6 and 15 K. All presented spectra were obtained using a modulation frequency and amplitude of 100 kHz and 10 G, respectively. Power- and temperature-dependent experiments were performed by adjusting the microwave power from 0.06325 to 20 mW at the indicated temperatures. Background signals were removed by baseline subtraction using IGOR Pro 9.00 (Wavemetrics). The difference spectra were generated by subtraction of the spectra of MarHDK without ATP from the spectra of MarHDK with ATP at the indicated powers. EPR spectral simulations of all spectra were carried out using the EasySpin Matlab toolbox[60]. Relative populations of the $S = ½$ and $S = 3/2$ signals in addition to the intermediates formed during turnover were determined by optimizing the weights of the different species at 15 K, where neither species was saturated. To simulate the inhomogeneous line broadening exhibited by the two species, g-strain values of [0.0008, 0.02, 0.055] ('E1(H)-like') and [0.024, 0.007, 0.045] ('E1(H)*-like') were included in the simulation. Spin quantitation was performed by integrating the baseline corrected experimental spectra of MarH and MarHDK without and with ATP under non-saturating conditions at 15 K. The total number of spins was then corrected to a concentration by comparison to a sample of Cu^{II}-azurin with a known concentration of 186 μM. The spin concentration was calculated based on the protein concentration of the enzyme complex to determine the spins per complex.

Cryo-EM grid preparation. Thermo Scientific Vitrobot Mark IV was used for cryo-EM specimen freezing. UltrAuFoil R1.2/1.3 grids were made hydrophilic by glow discharging in a Pelco easiGlow with 30 mA current for 2 min. Then, 3.5 μl of MarDK protein at 1.9 mg ml^{-1} in 25 mM Tris pH 7.4, 100 mM NaCl, 2 mM sodium dithionite was applied to a glow-discharged grid. While all protein preparations and activity assays were performed in an anaerobic chamber, the final step of cryo-EM grid preparation in the Vitrobot under 100% humidity for 3–4 s was performed in the presence of air, due to technical limitations. After this blotting step, the grid was plunged into liquid ethane cooled by liquid nitrogen. Then, the grids were stored in liquid nitrogen until examination. The brief duration ultimately exposed the sample to oxygen such that the system could be oxidatively damaged. Thus, as seen for N$_2$ase, the catalytic M-cluster can be lost to oxidative damage and the P-cluster can be oxidatively damaged such that one or more atoms are removed[28].

Cryo-EM data collection. Data were collected on a ThermoScientific Titan Krios G3i cryo-TEM operated at 300 kV and at a nominal 105,000 magnification using the ThermoScientific EPU program with a nominal defocus range of −1.0 μm to −2.0 μm. Image stack files were filtered with a BioQuantum energy filter at 15 eV slit width and acquired with a Gatan K3 Direct Electron Detector (Gatan) in Counted Super-Resolution mode at a pixel size of 0.4125 Å. Total electron dose was 50 e$^-$ Å^{-2}, and each stack file consisted of 40 frames.

Cryo-EM image processing. Images were processed exclusively using CryoSPARC[61] as shown in Extended Data Fig. Fig 4. The dataset was subjected to patch motion correction with an output F-crop factor of 1/2 resulting in a pixel size of 0.825 Å. Patch contrast transfer function estimation and contrast transfer function cut-off with vision screening at 4.05 Å were performed (removing less than 1% of micrographs, suggesting the high quality of data). Blob Picker was then performed, and particles were extracted into 64 × 64-pixel boxes at a pixel size of 3.3 Å, followed by two rounds of two-dimensional (2D) classification to generate templates for Template Picker. Nine unique classes representing unique views of the second 2D classification were selected as templates and applied to the selected micrographs using Template Picker. Particles were then inspected and extracted into 64 × 64-pixel boxes at a pixel size of 3.3 Å, followed by 2D classification. Ab initio three-dimensional (3D) reconstruction of ten classes was performed using selected particles, followed by heterogeneous refinement. The particles of the best class were used for further ab initio 3D reconstruction with three classes, followed by heterogeneous refinement. Three-dimensional classification of ten classes with a target resolution of 6 Å was applied to the best class of the ab initio reconstruction, and five of the ten 3D classes that showed complete structures were selected. The particles of the selected 3D classes were reextracted into 400 × 400-pixel boxes at a pixel size of 0.825 Å. Ab initio 3D reconstruction with three classes and heterogenous refinement was subsequentially applied to the reextracted particles. Two classes that showed complete structures were selected, combined and processed by non-uniform refinement, yielding the final map at 2.35 Å resolution based on the Fourier shell correlation global resolution plot at a Fourier shell correlation of 0.143 generated by CryoSPARC from final electron density map in Extended Data Fig. 4 (ref. 61).

MarDK model building and structure refinement. An ab initio model of a tetrameric MarDK complex was generated with AlphaFold-multimer (v.3)[62] as implemented in the AlphaFold colab notebook (v.1.5.2)[63]. N-terminal residues with a predicted random coil type conformation were truncated and the resultant model was placed into the cryo-EM map with phenix.dock_in_map[64]. Following model placement, discrepancies between the observed map and the predicted model were corrected with molecular dynamics flexible fitting using the ISOLDE plugin[65] in ChimeraX[66]. The MarDK model was further refined with phenix.real_space_refine[67] in combination with iterative real space refinement in Coot[68]. The final MarDK model was validated with MolProbity as implemented in the PHENIX software package[64].

For cluster modelling, P-cluster restraints were downloaded from the PDB in CIF format (ligand ID: CLF; https://www.rcsb.org/ligand/CLF), and phenix.elbow was used to convert the restraints, without geometry modification, into a format suitable for phenix.real_space_refine[67]. To reflect the oxidation state of the P-cluster, the Fe #8 atom was removed along with its angle and bond length restraints. The S1/FE6 bond length restraint was increased by 0.1 Å. The complete oxidized P-cluster restraint file used for model refinement is included as Supplementary Data 4. In addition, custom tetrahedral bond length and angle restraints for phenix.real_space_refine were defined between the sulfur atom of MarDK Cys residues and P-cluster Fe atoms to have an ideal bond length of 2.3 Å with a sigma value of 0.1 Å. These restraints are included in Supplementary Data 5.

For AlphaFold 3 models, Chai-1 was utilized to predict the location and coordination of a 4Fe-4S cluster, P-cluster (likely mar1 cluster) and L-cluster (likely mar2 cluster)[69], with SMILES strings of S12[Fe](S3[Fe]11)S([Fe]22)[Fe]3S12, S12[Fe](S([Fe]22)[Fe]3S42)S3([Fe]23)

([Fe]14)([Fe]1S22)[Fe](S33)S1[Fe]23 and S12[Fe](S([Fe]2S23)[Fe]33S4)(S33([Fe]567)([Fe]12S7)[Fe]14S62)S[Fe]3(S53)S1[Fe]32 used to represent the clusters, respectively. Bolz-1 and Chai-1 could not render a true L-cluster from a SMILES string, so an 'L-cluster' with a central sulfide was used and then the central sulfide replaced with a carbide.

Reporting summary

Further information on research design is available in the Nature Portfolio Reporting Summary linked to this article.

Data availability

Structural models and electron density maps are available through PDB ID 9D9U and EMDB ID EMD-46680. All other data are available from the authors upon reasonable request. Source data are provided with this paper.

References

1. Lomans, B., Van der Drift, C., Pol, A. & Op den Camp, H. Microbial cycling of volatile organic sulfur compounds. *CMLS* **59**, 575–588 (2002).
2. Hopkins, F. E., Archer, S. D., Bell, T. G., Suntharalingam, P. & Todd, J. D. The biogeochemistry of marine dimethylsulfide. *Nat. Rev. Earth Environ.* **4**, 361–376 (2023).
3. North, J. A., Miller, A. R., Wildenthal, J. A., Young, S. J. & Tabita, F. R. Microbial pathway for anaerobic 5′-methylthioadenosine metabolism coupled to ethylene formation. *Proc. Natl Acad. Sci. USA* **114**, E10455–E10464 (2017).
4. Hazelwood, L. A., Daran, J.-M., Van Maris, A. J., Pronk, J. T. & Dickinson, J. R. The Ehrlich pathway for fusel alcohol production: a century of research on *Saccharomyces cerevisiae* metabolism. *Appl. Environ. Microbiol.* **74**, 2259–2266 (2008).
5. North, J. A. et al. A nitrogenase-like enzyme system catalyzes methionine, ethylene, and methane biogenesis. *Science* **369**, 1094–1098 (2020).
6. Harris, D. F. et al. CO as a substrate and inhibitor of H+ reduction for the Mo-, V-, and Fe-nitrogenase isozymes. *J. Inorg. Biochem.* **213**, 111278 (2020).
7. Hoffman, B. M., Lukoyanov, D., Yang, Z.-Y., Dean, D. R. & Seefeldt, L. C. Mechanism of nitrogen fixation by nitrogenase: the next stage. *Chem. Rev.* **114**, 4041–4062 (2014).
8. Rutledge, H. L. & Tezcan, F. A. Electron transfer in nitrogenase. *Chem. Rev.* **120**, 5158–5193 (2020).
9. Muraki, N. et al. X-ray crystal structure of the light-independent protochlorophyllide reductase. *Nature* **465**, 110–114 (2010).
10. Nomata, J., Mizoguchi, T., Tamiaki, H. & Fujita, Y. A second nitrogenase-like enzyme for bacteriochlorophyll biosynthesis: reconstitution of chlorophyllide a reductase with purified X-protein (BchX) and YZ-protein (BchY-BchZ) from *Rhodobacter capsulatus*. *J. Biol. Chem.* **281**, 15021–15028 (2006).
11. Zheng, K., Ngo, P. D., Owens, V. L., Yang, X.-P. & Mansoorabadi, S. O. The biosynthetic pathway of coenzyme F430 in methanogenic and methanotrophic archaea. *Science* **354**, 339–342 (2016).
12. Ghebreamlak, S. M. & Mansoorabadi, S. O. Divergent members of the nitrogenase superfamily: tetrapyrrole biosynthesis and beyond. *ChemBioChem.* **21**, 1723–1728 (2020).
13. Burén, S., Jiménez-Vicente, E., Echavarri-Erasun, C. & Rubio, L. M. Biosynthesis of nitrogenase cofactors. *Chem. Rev.* **120**, 4921–4968 (2020).
14. Hu, Y. & Ribbe, M. W. Nitrogenase and homologs. *JBIC* **20**, 435–445 (2015).
15. Einsle, O. & Rees, D. C. Structural enzymology of nitrogenase enzymes. *Chem. Rev.* **120**, 4969–5004 (2020).
16. Wiig, J. A., Hu, Y., Lee, C. C. & Ribbe, M. W. Radical SAM-dependent carbon insertion into the nitrogenase M-cluster. *Science* **337**, 1672–1675 (2012).
17. Vazquez Ramos, J. et al. Characterization of the iron–sulfur clusters in the nitrogenase-like reductase CfbC/D required for coenzyme F430 biosynthesis. *FEBS J.* **291**, 3233–3248 (2024).
18. Kiesel, S. et al. Iron-sulfur cluster-dependent catalysis of chlorophyllide a oxidoreductase from *Roseobacter denitrificans*. *J. Biol. Chem.* **290**, 1141–1154 (2015).
19. Ludden, P. W. & Burris, R. H. Purification and properties of nitrogenase from *Rhodospirillum rubrum*, and evidence for phosphate, ribose and an adenine-like unit covalently bound to the iron protein. *Biochem. J.* **175**, 251–259 (1978).
20. Jiménez-Vicente, E. et al. Application of affinity purification methods for analysis of the nitrogenase system from Azotobacter vinelandii. *Methods Enzymol.* **613**, 231–255 (2018).
21. Dodsworth, J. A. & Leigh, J. A. Regulation of nitrogenase by 2-oxoglutarate-reversible, direct binding of a PII-like nitrogen sensor protein to dinitrogenase. *Proc. Natl Acad. Sci. USA* **103**, 9779–9784 (2006).
22. Ludden, P. W. Reversible ADP-ribosylation as a mechanism of enzyme regulation in procaryotes. *Mol. Cell. Biochem.* **138**, 123–129 (1994).
23. Harris, D. F. et al. Mechanism of N_2 reduction catalyzed by Fe-nitrogenase involves reductive elimination of H_2. *Biochemistry* **57**, 701–710 (2018).
24. Favier-Teodorescu, L., Cornet, J.-F. & Dussap, C. G. Modelling continuous culture of Rhodospirillum rubrum in photobioreactor under light limited conditions. *Biotechnol. Lett.* **25**, 359–364 (2003).
25. Kirn, J. & Rees, D. Crystallographic structure and functional implications of the nitrogenase molybdenum–iron protein from Azotobacter vinelandii. *Nature* **360**, 553–560 (1992).
26. Schmidt, F. V. et al. Structural insights into the iron nitrogenase complex. *Nat. Struct. Mol. Biol.* **31**, 150–158 (2024).
27. Trncik, C., Detemple, F. & Einsle, O. Iron-only Fe-nitrogenase underscores common catalytic principles in biological nitrogen fixation. *Nat. Catal.* **6**, 415–424 (2023).
28. Rutledge, H. L., Field, M. J., Rittle, J., Green, M. T. & Tezcan, F. A. Role of serine coordination in the structural and functional protection of the nitrogenase P-cluster. *J. Am. Chem. Soc.* **144**, 22101–22112 (2022).
29. Rutledge, H. L. et al. Redox-dependent metastability of the nitrogenase P-cluster. *J. Am. Chem. Soc.* **141**, 10091–10098 (2019).
30. Owens, C. P., Katz, F. E., Carter, C. H., Oswald, V. F. & Tezcan, F. A. Tyrosine-coordinated P-cluster in G. diazotrophicus nitrogenase: evidence for the importance of O-based ligands in conformationally gated electron transfer. *J. Am. Chem. Soc.* **138**, 10124–10127 (2016).
31. Keable, S. M. et al. Structural characterization of the P1+ intermediate state of the P-cluster of nitrogenase. *J. Biol. Chem.* **293**, 9629–9635 (2018).
32. Kent, H. M., Ioannidis, I., Gormal, C., Smith, B. E. & Buck, M. Site-directed mutagenesis of the *Klebsiella pneumoniae* nitrogenase. Effects of modifying conserved cysteine residues in the α-and β-subunits. *Biochem. J.* **264**, 257–264 (1989).
33. Einsle, O. Catalysis and structure of nitrogenases. *Curr. Opin. Struct. Biol.* **83**, 102719 (2023).
34. Bulen, W. & LeComte, J. The nitrogenase system from *Azotobacter*: two-enzyme requirement for N2 reduction, ATP-dependent H2 evolution, and ATP hydrolysis. *Proc. Natl Acad. Sci. USA* **56**, 979 (1966).
35. Van Stappen, C. et al. The spectroscopy of nitrogenases. *Chem. Rev.* **120**, 5005–5081 (2020).
36. Yang, K.-Y., Haynes, C. A., Spatzal, T., Rees, D. C. & Howard, J. B. Turnover-dependent inactivation of the nitrogenase MoFe-protein at high pH. *Biochemistry* **53**, 333–343 (2014).

37. Lee, C. C., Hu, Y. & Ribbe, M. W. Unique features of the nitrogenase VFe protein from Azotobacter vinelandii. *Proc. Natl Acad. Sci. USA* **106**, 9209–9214 (2009).
38. Lindahl, P. et al. EPR, and magnetization studies of the *Azotobacter vinelandii* Fe protein. Evidence for a [4Fe-4S] 1+ cluster with spin S= 3/2. *J. Biol. Chem.* **260**, 11160–11173 (1985).
39. Blank, M. A. et al. Structural models of the [Fe4S4] clusters of homologous nitrogenase Fe proteins. *Inorg. Chem.* **50**, 7123–7128 (2011).
40. Ribbe, M. W. et al. Nitrogenase Fe protein: a multi-tasking player in substrate reduction and metallocluster assembly. *Molecules* **27**, 6743 (2022).
41. Schneider, K., Gollan, U., Dröttboom, M., Selsemeier-Voigt, S. & Müller, A. Comparative biochemical characterization of the iron-only nitrogenase and the molybdenum nitrogenase from *Rhodobacter capsulatus*. *Eur. J. Biochem.* **244**, 789–800 (1997).
42. Yang, Z.-Y. et al. The electronic structure of FeV-cofactor in vanadium-dependent nitrogenase. *Chem. Sci. J.* **12**, 6913–6922 (2021).
43. Rivera-Ortiz, J. M. & Burris, R. H. Interactions among substrates and inhibitors of nitrogenase. *J. Bacteriol.* **123**, 537–545 (1975).
44. Rohde, M., Laun, K., Zebger, I., Stripp, S. T. & Einsle, O. Two ligand-binding sites in CO-reducing V nitrogenase reveal a general mechanistic principle. *Sci. Adv.* **7**, eabg4474 (2021).
45. Jasper, J. et al. Chimeric interaction of nitrogenase-like reductases with the MoFe protein of nitrogenase. *ChemBioChem* **21**, 1733 (2020).
46. Park, S. C., Kwak, Y. M., Song, W. S., Hong, M. & Yoon, S.-I. Structural basis of effector and operator recognition by the phenolic acid-responsive transcriptional regulator PadR. *Nucleic Acids Res.* **45**, 13080–13093 (2017).
47. Medina, M. S. et al. CowN sustains nitrogenase turnover in the presence of the inhibitor carbon monoxide. *J. Biol. Chem.* **296**, 100501 (2021).
48. Chatterjee, R., Ludden, P. W. & Shah, V. K. Characterization of VnfG, the δ subunit of the vnf-encoded apodinitrogenase from *Azotobacter vinelandii*: implications for its role in the formation of functional dinitrogenase 2. *J. Biol. Chem.* **272**, 3758–3765 (1997).
49. Schlesier, J., Rohde, M., Gerhardt, S. & Einsle, O. A conformational switch triggers nitrogenase protection from oxygen damage by Shethna protein II (FeSII). *J. Am. Chem. Soc.* **138**, 239–247 (2016).
50. Narehood, S. M. et al. Structural basis for the conformational protection of nitrogenase from O_2. *Nature* **637**, 991–997 (2025).
51. Franke, P., Freiberger, S., Zhang, L. & Einsle, O. Conformational protection of molybdenum nitrogenase by Shethna protein II. *Nature* **637**, 998–1004 (2025).
52. Wolle, D., Kim, C., Dean, D. & Howard, J. Ionic interactions in the nitrogenase complex. Properties of Fe-protein containing substitutions for Arg-100. *J. Biol. Chem.* **267**, 3667–3673 (1992).
53. Lukoyanov, D. A. et al. The one-electron reduced active-site FeFe-cofactor of Fe-nitrogenase contains a hydride bound to a formally oxidized metal-ion core. *Inorg. Chem.* **61**, 5459–5464 (2022).
54. Munk, A. C. et al. Complete genome sequence of Rhodospirillum rubrum type strain (S1 T). *SIGS* **4**, 293–302 (2011).
55. Ormerod, J. G., Ormerod, K. S. & Gest, H. Light-dependent utilization of organic compounds and photoproduction of molecular hydrogen by photosynthetic bacteria; relationships with nitrogen metabolism. *Arch. Biochem. Biophys.* **94**, 449–463 (1961).
56. Kovach, M. E. et al. Four new derivatives of the broad-host-range cloning vector pBBR1MCS, carrying different antibiotic-resistance cassettes. *Gene* **166**, 175–176 (1995).
57. Hessner, M. J., Wejksnora, P. J. & Collins, M. Construction, characterization, and complementation of Rhodospirillum rubrum puf region mutants. *J. Bacteriol.* **173**, 5712–5722 (1991).
58. Lee, C. C., Ribbe, M. W. & Hu, Y. Purification of nitrogenase proteins. *Methods Mol. Biol.* **1876**, 111–124 (2019).
59. Dzieciatkowska, M., Hill, R. & Hansen, K. C. GeLC-MS/MS analysis of complex protein mixtures. *Methods Mol. Biol.* **1156**, 53–66 (2014).
60. Stoll, S. & Schweiger, A. EasySpin, a comprehensive software package for spectral simulation and analysis in EPR. *J. Magn. Reson.* **178**, 42–55 (2006).
61. Punjani, A., Rubinstein, J. L., Fleet, D. J. & Brubaker, M. A. cryoSPARC: algorithms for rapid unsupervised cryo-EM structure determination. *Nat. Methods* **14**, 290–296 (2017).
62. Evans, R. et al. Protein complex prediction with AlphaFold-Multimer. Preprint at *bioRxiv* https://doi.org/10.1101/2021.10.04.463034 (2022).
63. Mirdita, M. et al. ColabFold: making protein folding accessible to all. *Nat. Methods* **19**, 679–682 (2022).
64. Liebschner, D. et al. Macromolecular structure determination using X-rays, neutrons and electrons: recent developments in Phenix. *Acta Crystallogr. D* **75**, 861–877 (2019).
65. Croll, T. I. ISOLDE: a physically realistic environment for model building into low-resolution electron-density maps. *Acta Crystallogr. Sect. D* **74**, 519–530 (2018).
66. Goddard, T. D. et al. UCSF ChimeraX: meeting modern challenges in visualization and analysis. *Protein Sci.* **27**, 14–25 (2018).
67. Afonine, P. V. et al. Real-space refinement in PHENIX for cryo-EM and crystallography. *Acta Crystallogr. D* **74**, 531–544 (2018).
68. Casañal, A., Lohkamp, B. & Emsley, P. Current developments in Coot for macromolecular model building of electron cryo-microscopy and crystallographic data. *Protein Sci.* **29**, 1055–1064 (2020).
69. Boitreaud, J. et al. Chai-1: decoding the molecular interactions of life. Preprint at *bioRxiv* https://doi.org/10.1101/2024.10.10.615955 (2024).
70. Pence, N., Lewis, N., Alleman, A. B., Seefeldt, L. C. & Peters, J. W. Revealing a role for the G subunit in mediating interactions between the nitrogenase component proteins. *J. Inorg. Biochem.* **214**, 111273 (2021).
71. Warmack, R. A. et al. Structural consequences of turnover-induced homocitrate loss in nitrogenase. *Nat. Comm.* **14**, 1091 (2023).
72. Bröcker, M. J. et al. Crystal structure of the nitrogenase-like dark operative protochlorophyllide oxidoreductase catalytic complex (ChlN/ChlB). *J. Biol. Chem.* **285**, 27336–27345 (2010).
73. Scheres, S. H. RELION: implementation of a Bayesian approach to cryo-EM structure determination. *J. Struct. Biol.* **180**, 519–530 (2012).
74. Asarnow, D., Palovcak, E. & Cheng, Y. UCSF pyem v0. 5. *Zenodo* https://doi.org/10.5281/zenodo.3576630 (2019).

Acknowledgements

We thank S. C. Jantzi, Plasma Chemistry Laboratory, Center for Applied Isotope Studies, University of Georgia for ICP-MS assistance. We thank L. Zhang of the Ohio State University Campus Chemical Instrument Facility for proteomics assistance. This work was supported by the Department of Energy, Office of Science, Biological and Environmental Research Program (grant no. DE-SC0022091 to J.A.N.); by the Department of Energy, Office of Science, Basic Energy Sciences, Physical Biosciences Program (grant no. DE-SC0024125 to J.A.N. and H.S.S.). The work (proposal: 10.46936/10.25585/60001264) conducted by the U.S. Department of Energy Joint Genome Institute (https://ror.org/04xm1d337), a DOE Office of Science User Facility, is supported by the Office of Science of the U.S. Department of Energy operated under contract no. DE-AC02-05CH11231. This research used resources from the Laboratory for BioMolecular Structures, which is supported by the US DOE, Office of Science, Office of Biological and Environmental Research (grant no. KP1607011).

Author contributions

J.A.N., H.S.S., Y.Y. and S.M. conceived, initiated, coordinated and supervised the research and acquired funding. S.M., J.A.N., S.A.F., E.M.B. and K.M.B. performed cell growth, protein purification and activity assays. S.M., J.A.N., A.A.C. and O.G.W. performed cloning, genetic manipulation and chromatographic analysis of bacterial metabolism. L.C.L. and H.S.S. performed and analysed EPR experiments. G.H. and D.F.K. collected and processed cryo-EM data and built the structure model. The manuscript was written by J.A.N., H.S.S., G.H., D.F.K. and L.C.L. All authors assisted in analysing data, discussing the results and editing the manuscript.

Competing interests

The authors declare no competing interests.

Additional information

Extended data is available for this paper at https://doi.org/10.1038/s41929-025-01425-3.

Supplementary information The online version contains supplementary material available at https://doi.org/10.1038/s41929-025-01425-3.

Correspondence and requests for materials should be addressed to Justin A. North.

Peer review information *Nature Catalysis* thanks Oliver Einsle and the other, anonymous, reviewer(s) for their contribution to the peer review of this work.

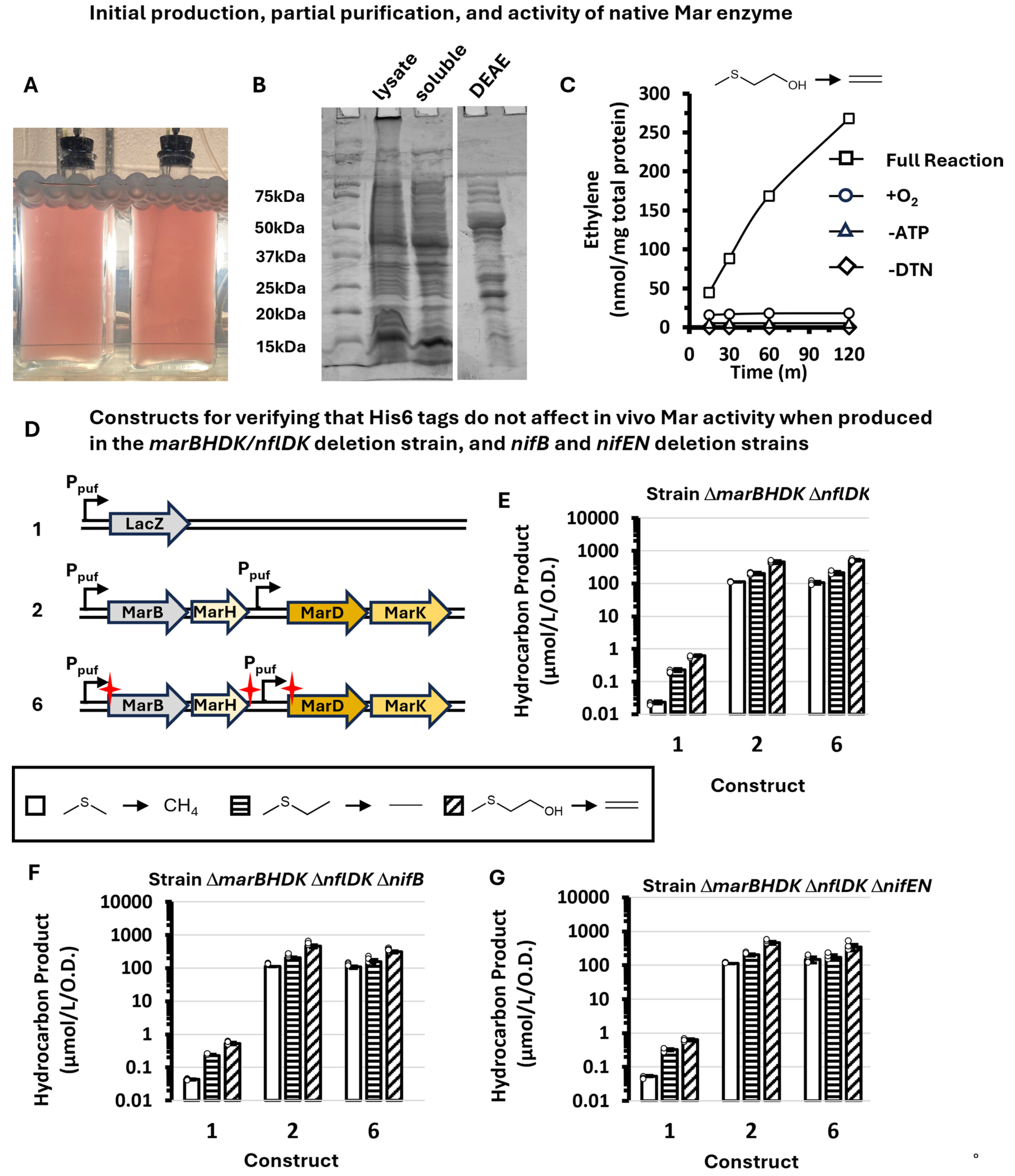

Extended Data Fig. 1 | MAR Purification. A) Anaerobic phototrophic growth of wild type *R. rubrum* in 2 L roux bottles. **B**) Lysate, soluble fraction, and DEAE fraction containing MAR natively purified from wild type *R. rubrum*. Experiments were conducted n = 2 times with similar results. **C**) Activity and functional requirements of native MAR activity in the DEAE fraction (B) for n = 1 sample. All reactions unless otherwise indicated contained 4 mM ATP, 6 mM dithionite, 1 mM MT-EtOH, and ATP regeneration system. **D**) Plasmid-based MAR gene expression system. Red stars indicate location of poly-histidine sequences. **E-G**) Total hydrocarbons produced when MAR gene constructs in (**D**) are expressed in the *marBHDK*, *nflDK*, *nifB*, and *nifEN* deletion strain to verify histidine tags do not alter in vivo activity. Previously it was shown that the *nflDK* genes of unknown function are not involved in MAR activity[5]. Plasmid 1, pPUF-MCS3; 2, pPUF-M4; 3, pPUF-MarB$_{\text{His6}}$-MarH$_{\text{His6}}$-MarD$_{\text{His6}}$-MarK (Supplementary Table 2). In E-G averages and standard deviation error bars are for n = 3 independent experiments.

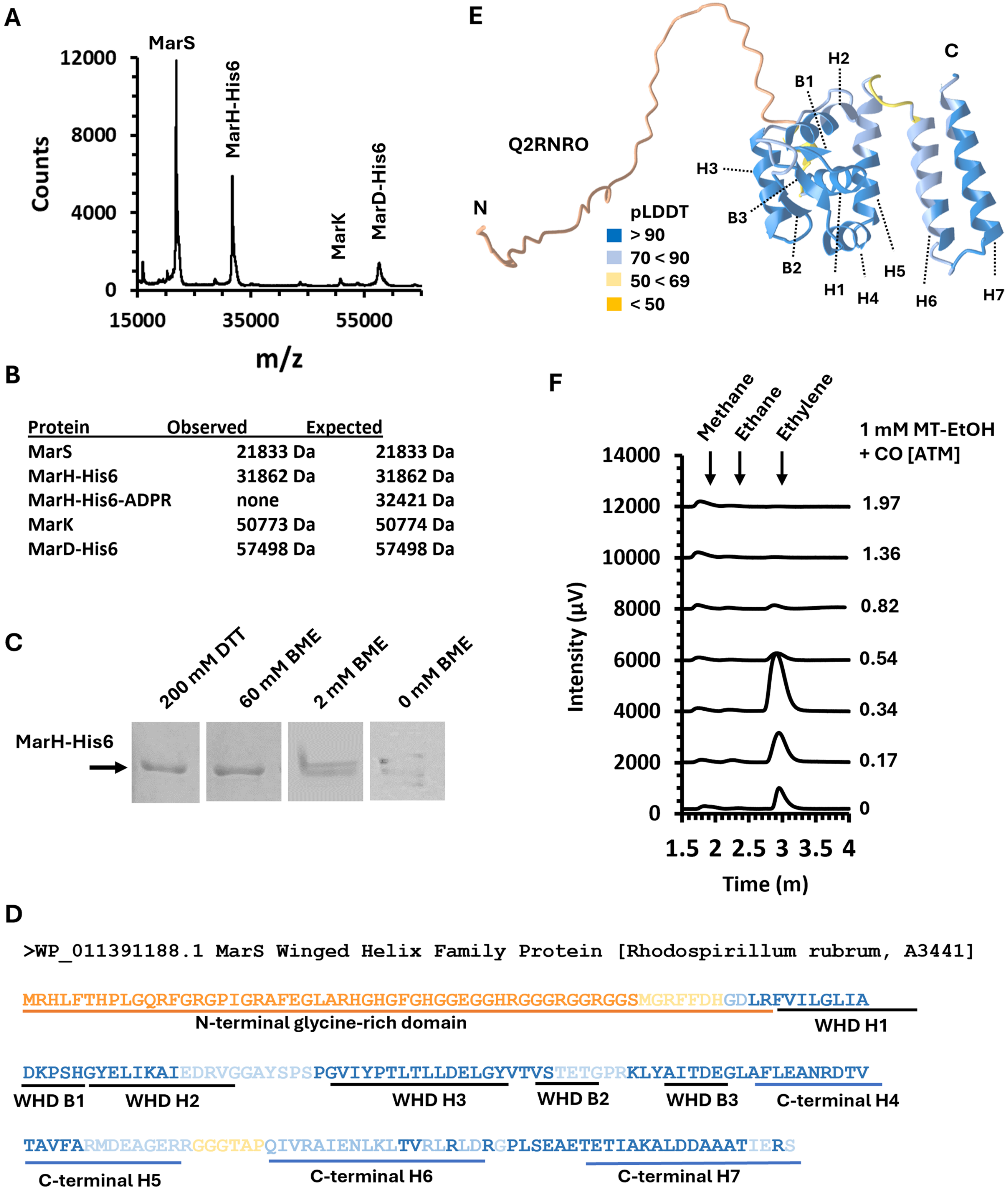

Protein	Observed	Expected
MarS	21833 Da	21833 Da
MarH-His6	31862 Da	31862 Da
MarH-His6-ADPR	none	32421 Da
MarK	50773 Da	50774 Da
MarD-His6	57498 Da	57498 Da

```
>WP_011391188.1 MarS Winged Helix Family Protein [Rhodospirillum rubrum, A3441]

MRHLFTHPLGQRFGRGPIGRAFEGLARHGHGFGHGGEGGHRGGGRGGRGGSMGRFFDHGDLRFVILGLIA
DKPSHGYELIKAIEDRVGGAYSPSPGVIYPTLTLLDELGYVTVSTETGPRKLYAITDEGLAFLEANRDTV
TAVFARMDEAGERRGGGTAPQIVRAIENLKLTVRLRLDRGPLSEAETETIAKALDDAAATIERS
```

Extended Data Fig. 2 | MAR Characterization. A-B) Maldi-TOF mass spectrometry of isolated MarH and MarDK + A3441 protein from DEAE chromatography (Fig. 2). ADPR; ADP-ribose post-translational modification. Experiments conducted for n = 2 samples with same results. **C**) SDS-page gel electrophoresis of MarH from size exclusion purification (Fig. 2) under varying reducing conditions. **D-E**) AlphaFold predicted structure (UniProt: Q2RNRO) and sequence of the A3441 protein colored by predicted local density difference test. A3441 contains a predicted winged helix domain and a C-terminal helical domain homologous to other winged-helix DNA- and protein-binding dimeric regulatory proteins. In addition, it contains a glycine-rich (31%) N-terminal domain. **F**) Gas chromatography analysis for Fig. 3f of MarHDK activity in the presence of CO showing that CO is not reduced to methane or other hydrocarbons by MAR.

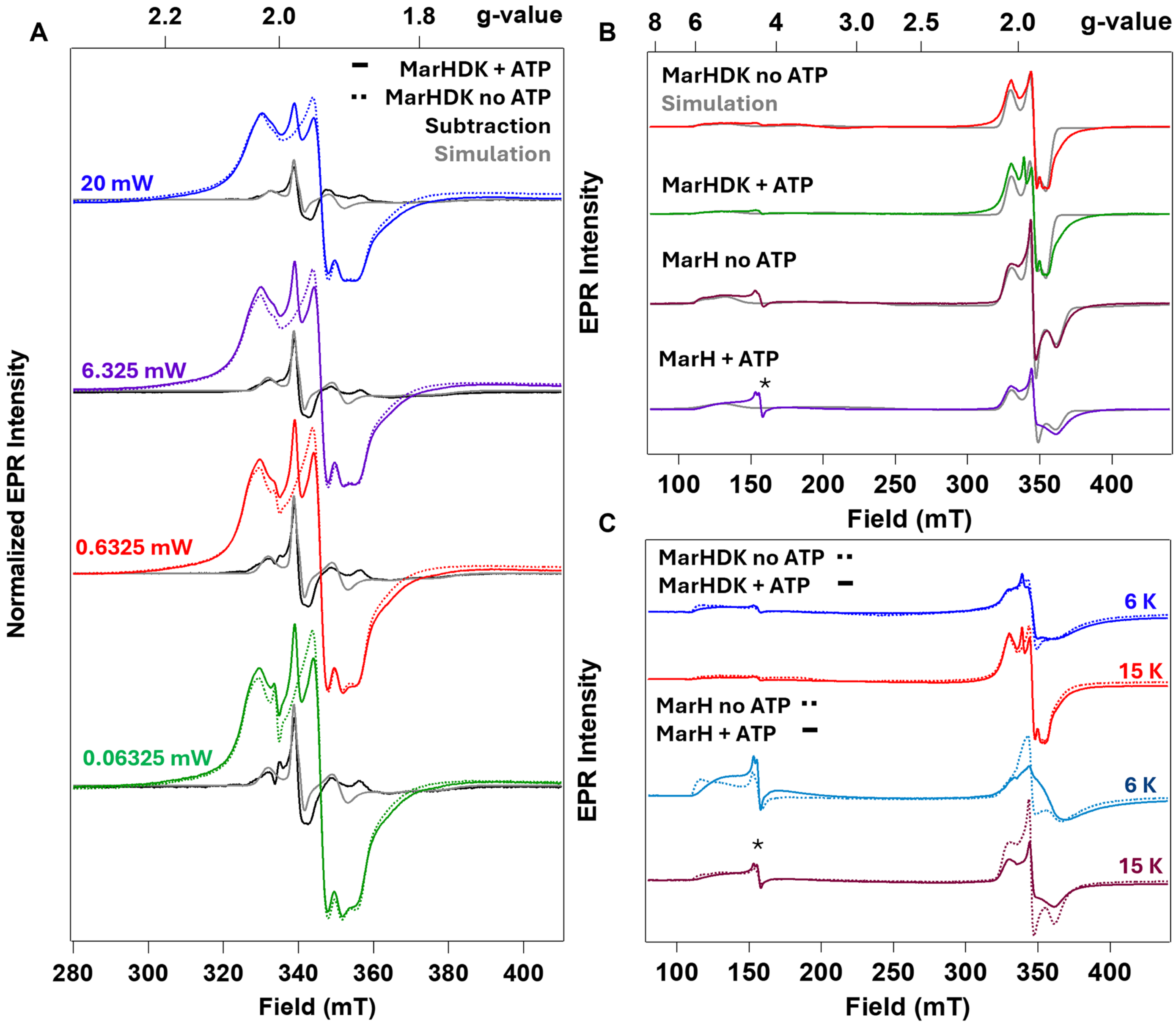

D	g_1[a] S= 1/2	g_2[a] S= 1/2	g_3[a] S= 1/2	E/D[a] S= 3/2	Population[a] S = ½ (%)	Protein Concentration (mg/mL)	Spins/ complex[b]
MarH no ATP	2.03	1.95	1.85	0.21	18	28	0.48
MarH + ATP	2.03	1.93	1.85	0.25	17	28	0.34
MarHDK no ATP	2.03	1.94	1.89	0.21	26	30	1.16
MarHDK + ATP	2.03	1.94	1.89	0.25	33	30	1.07

Extended Data Fig. 3 | Spectroscopic characterization of MAR metallocofactors. A) CW X-band EPR spectra (ν = 9.38 GHz) of MarHDK. Isolated MarHDK enzyme (135 µM MarH dimer + 70 µM MarDK tetramer) without ATP *(dashed)*, with ATP (*solid*), and subtraction of resting-state from turnover signal (*black*) with simulated signals arising from "E1(H)-like" and "E1(H)*-like" species (*gray*). Spectral intensities are normalized for power. Spectra were collected at T = 15.0 K at the indicated powers. **B)** Isolated MarHDK enzyme (135 µM MarH dimer + 70 µM MarDK tetramer without ATP (*red*) and with ATP (*green*). Isolated MarH protein dimer (435 µM) without ATP (*maroon*), and with ATP (*purple*). Associated simulations (*gray*) for the S = ½ and S = 3/2 signals at 15.0 K, $P_{\mu w}$ = 20 mW. * indicates adventitiously bound iron **C)** Isolated MarHDK enzyme (135 µM MarH dimer + 70 µM MarDK tetramer) at 6 K (blue) and 15 K (red), and isolated MarH protein dimer (435 µM) at 6 K (cyan) and 15 K (maroon) without ATP (*dashed*) and with ATP (*solid*) with $P_{\mu w}$ = 20 mW. Temperature dependence of S = 3/2 signals in samples without ATP indicate population of $m_s \pm ½$ Kramer's doublet at higher temperature, leading to an assignment of D < 0. * indicates adventitiously bound iron. **D)** Simulated spin Hamiltonian parameters and corresponding spin quantitation numbers for MarH and MarHDK with and without ATP. a: Values determined from simulation parameters of experimental spectrum with S = ½ and S = 3/2 species. b. Determined from spin quantitation with 186 µM Cu^{II}-azurin. EPR experiments were conducted n = 2 times with similar results.

https://doi.org/10.1038/s41929-025-01425-3

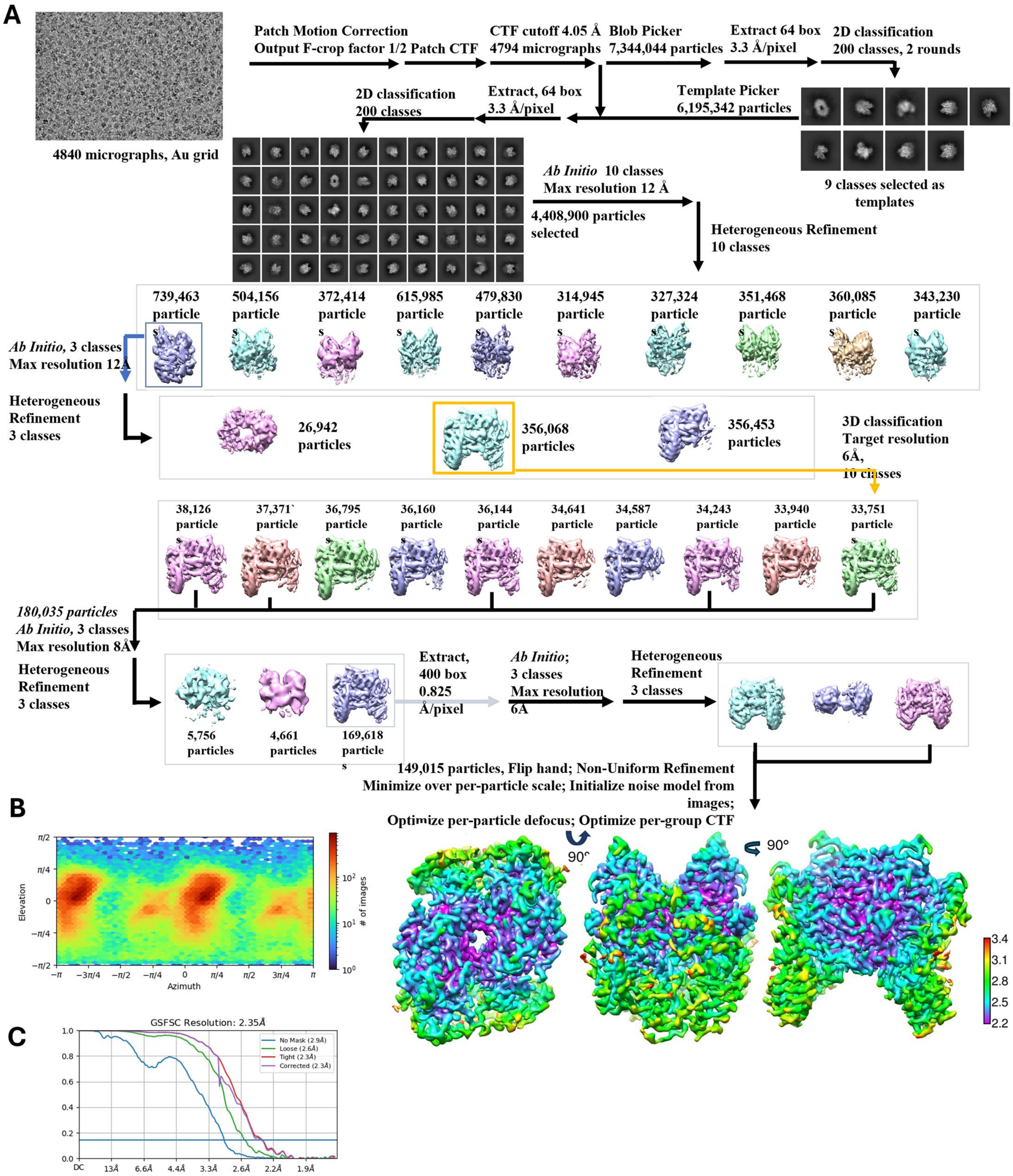

Extended Data Fig. 4 | Image processing workflow for Cryo-EM data. **A**) Cryo-EM data processing workflow using CryoSPARC v4.2.1. The 3D maps were displayed using UCSF ChimeraX[66,73,74]. The false color scale indicates the local resolution **B**) Orientation distribution of particles that produced the final electron density map in (**A**). **C**) Fourier Shell Correlation global resolution plot at FCS = 0.143 generated by CryoSPARC for final electron density map in (**A**).

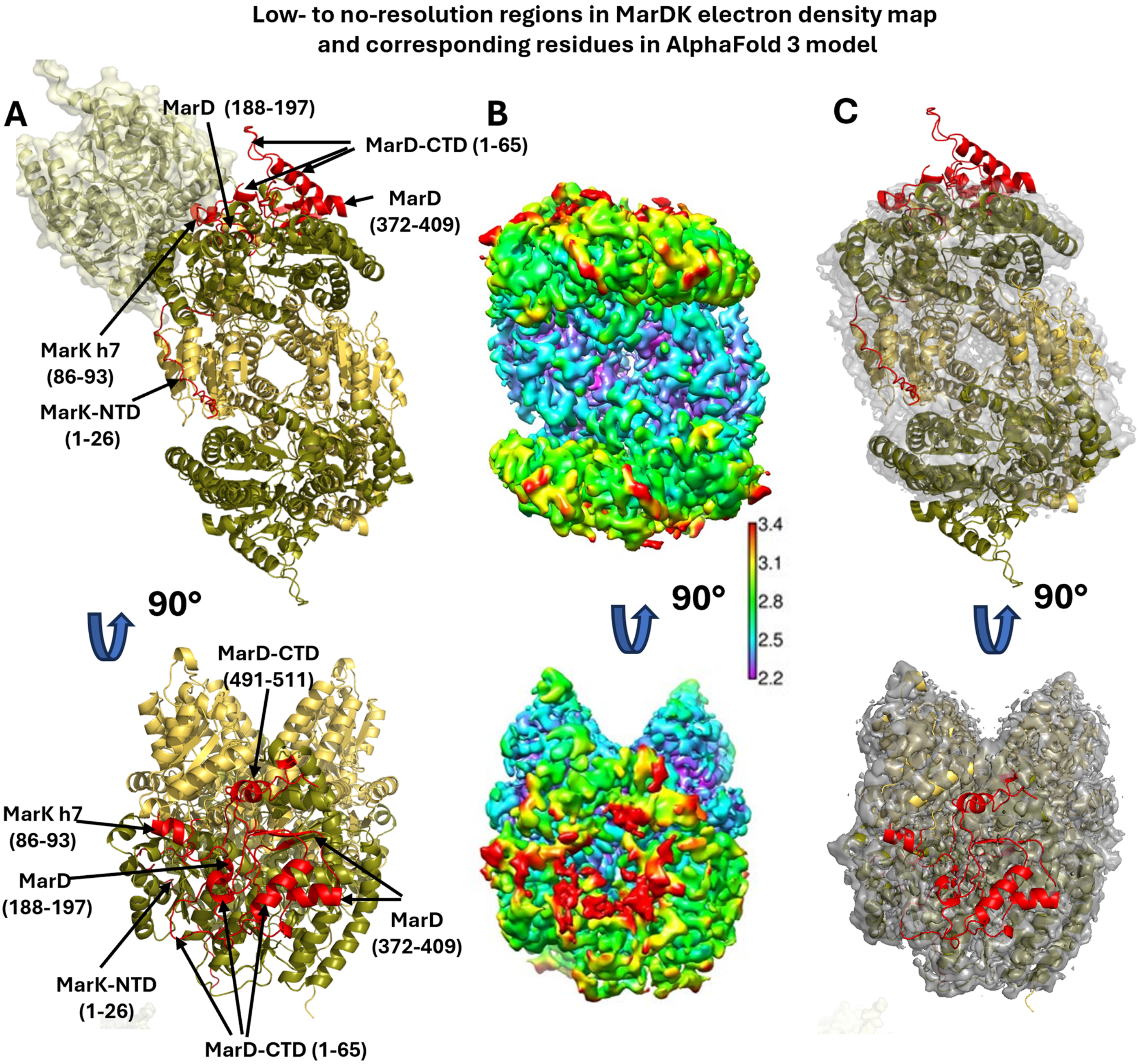

Extended Data Fig. 5 | Comparison of CryoEM map of MarDK to AlphaFold 3 models. A) AlphaFold 3 predicted locations for MarD residues 1-65, 188-197, and 372-409 and MarK residues 1-26 and 88-93. MarK helix h7 (residues 86-93) and MarD residues 188-197 are predicted to reside under and adjacent to MarH when bound (as shown in panel **A**). Theses correspond to a lower (< 3.5 Å) to no-resolution region in the Cryo-EM map in panel **B**. **B**) Local resolution plot of the final Cryo-EM map for MarDK from Extended Data Fig. 4 at a relatively lower threshold showing the lower- to no-resolution region at the MarD surface. **C**) Overlay of Cryo-EM electron density map (from **B**; in gray) and AlphaFold 3 model (from **A**).

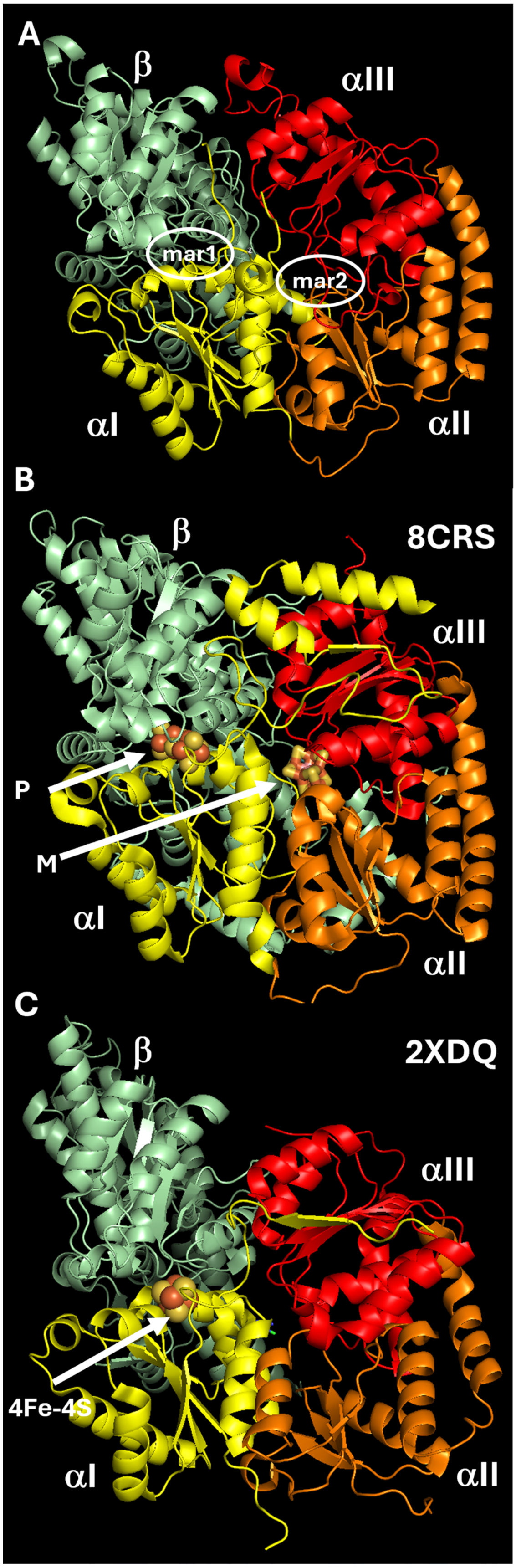

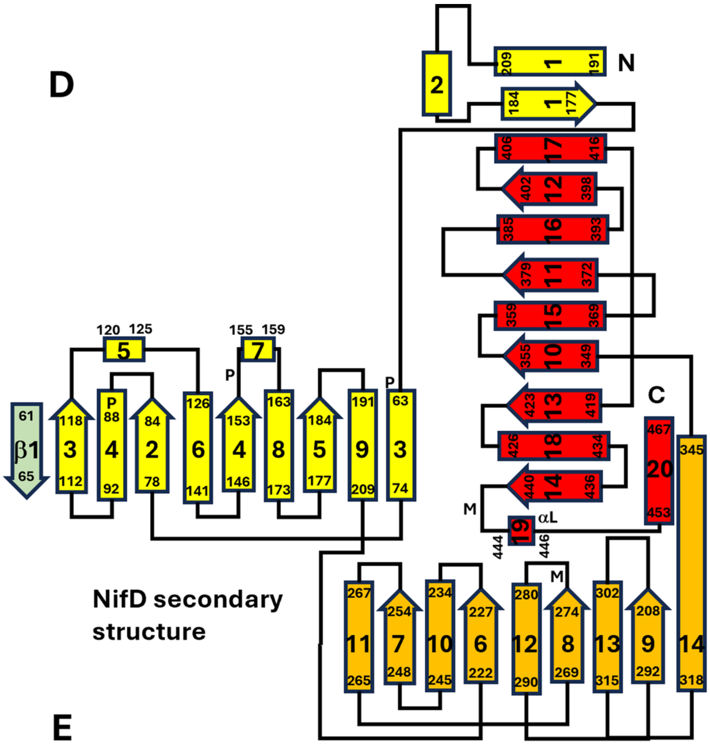

E

Domain	NifD (A. vinelandii) Start	Stop	feature	#	MarD (R. rubrum) Start	Stop	feature	#	ChlN (T. vestitus) Start	Stop	feature
I	5	19	α helix	1	13	17	α helix	1			
I	22	30	α helix	2	22	25	β sheet	1			
I	31	35	β sheet	1	27	42	α helix	2	10	15	β sheet
I	63	74	α helix	3	67	75	α helix	3	22	34	α helix
I	78	84	β sheet	2	81	86	β sheet	2	37	42	β sheet
I	88	92	α helix	4	89	108	α helix	4	44	55	α helix
I									57	61	α helix
I	112	117	β sheet	3	114	119	β sheet	3	64	69	β sheet
I	120	125	α helix	5	126	130	α helix	5	71	77	α helix
I	128	141	α helix	6	132	147	α helix	6	80	97	α helix
I	146	153	β sheet	4	151	157	β sheet	4	100	105	β sheet
I	155	159	α helix	7	159	163	α helix	7	106	112	α helix
I	163	173	α helix	8	167	178	α helix	8	115	128	α helix
I	177	184	β sheet	5	181	187	β sheet	5	131	135	β sheet
I	191	209	α helix	9	194	209	α helix	9	144	156	α helix
II	222	227	β sheet	6	222	227	β sheet	6	199	203	β sheet
II	234	245	α helix	10	233	240	α helix	10	206	220	α helix
II	248	254	β sheet	7	244	250	β sheet	7	224	229	β sheet
II	257	265	α helix	11	255	253	α helix	11	232	236	α helix
II	269	274	β sheet	8	264	269	β sheet	8	243	247	β sheet
II	280	290	α helix	12	275	285	α helix	12	252	264	α helix
II	292	298	β sheet	9	287	291	β sheet	9	265	269	β sheet
II	302	315	α helix	13	297	312	α helix	13	274	260	α helix
II	318	345	α helix	14	317	339	α helix	14	297	316	α helix
III	349	355	β sheet	10	346	350	β sheet	10	319	322	β sheet
III	359	369	α helix	15	352	363	α helix	15	328	339	α helix
III	372	379	β sheet	11	369	373	β sheet	11	342	348	β sheet
III	385	393	α helix	16	389	397	α helix	16	357	370	α helix
III	398	402	β sheet	12	401	405	β sheet	12	375	379	β sheet
III	406	416	α helix	17	409	420	α helix	17	382	394	α helix
III	419	423	β sheet	13	423	427	β sheet	13	397	400	β sheet
III	426	434	α helix	18	433	439	α helix	18	401	410	α helix
III	436	440	β sheet	14	442	446	β sheet	14	414	417	β sheet
III	444	446	αL helix	19							
III	453	467	α helix	20	455	479	α helix	19	419	424	α helix
III					488	491	α helix	20	428	449	α helix

Extended Data Fig. 6 | Alpha subunit domain structure and residue numbering. Structures colored by domain for **A**) MarD, **B**) NifD, and **C**) DPOR ChlN. **D**) NifD secondary structure and **E**) enumeration of secondary structure based off Kim et al, 1992, Nature[25]. For MarD, cream highlighted cells indicate regions of poor resolution in Cryo-EM structure (Extended Data Fig. 5) and are inferred from AlphaFold 3 model.

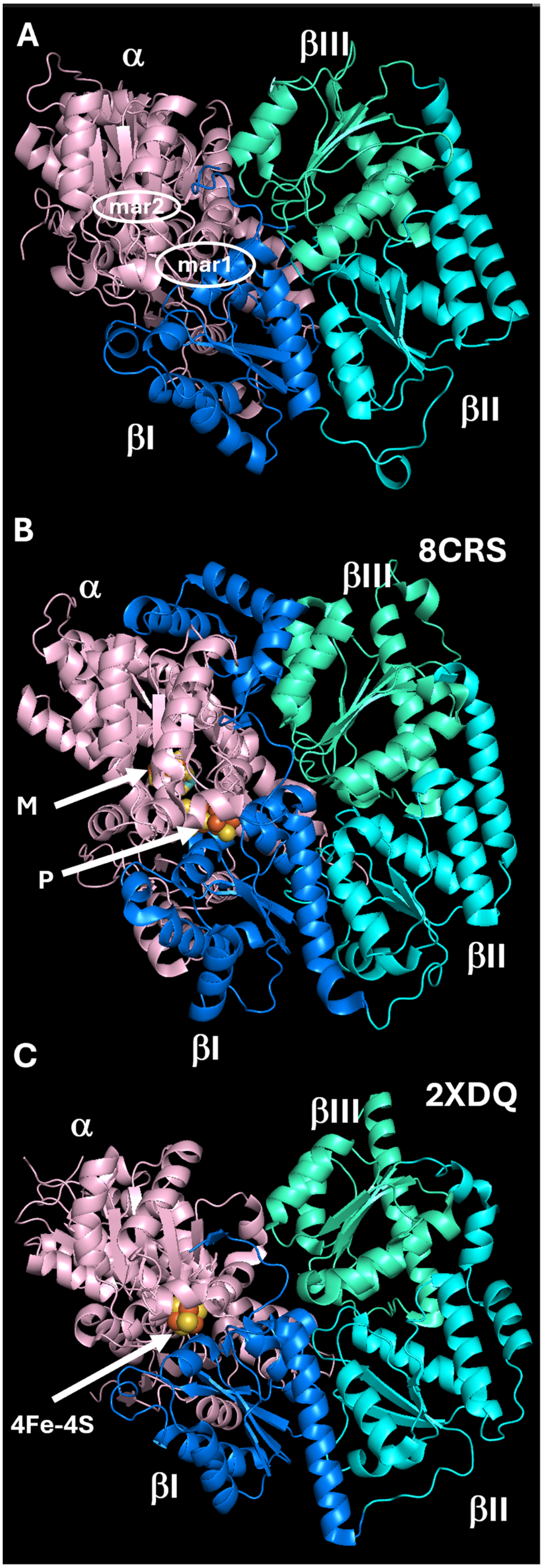

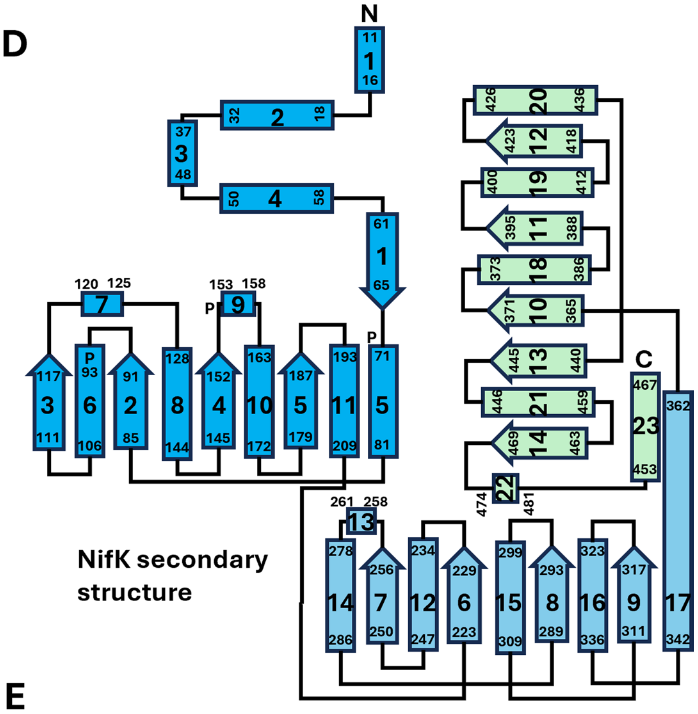

E

	NifK (A. vinelandii)				MarK (R. rubrum)				ChlB (T. vestitus)		
Domain	Start	Stop	feature	#	Start	Stop	feature	#	Start	Stop	feature
I	11	16	α helix	1							
I	18	32	α helix	2							
I	37	48	α helix	3							
I	50	58	α helix	4							
I	61	65	β sheet	1	24	27	β sheet	1	2	5	β sheet
I	71	81	α helix	5	33	42	α helix	1	11	21	α helix
I	85	91	β sheet	2	46	51	β sheet	2	26	31	β sheet
I	93	106	α helix	6	56	65	α helix	2	37	48	α helix
I					74	77	α helix	3			
I	111	117	β sheet	3	79	84	β sheet	3	55	59	β sheet
I	120	125	α helix	7	88	92	α helix	4	62	66	α helix
I	128	142	α helix	8	96	109	α helix	5	71	85	α helix
I	145	152	β sheet	4	114	119	β sheet	4	88	92	β sheet
I	153	158	α helix	9	122	126	α helix	6	94	99	α helix
I	162	172	α helix	10	130	141	α helix	7	104	111	α helix
I	179	187	β sheet	5	144	149	β sheet	5	115	119	β sheet
I	193	209	α helix	11	156	171	α helix	8	130	153	α helix
II					177	181	α helix	9			
II	223	229	β sheet	6	187	191	β sheet	6	165	171	β sheet
II	234	247	α helix	12	201	215	α helix	10	177	193	α helix
II	250	256	β sheet	7	218	222	β sheet	7	195	201	β sheet
II	258	261	α helix	13							
II	278	286	α helix	14	230	239	α helix	11	208	215	α helix
II	289	293	β sheet	8	241	245	β sheet	8	217	221	β sheet
II	299	309	α helix	15	251	261	α helix	12	226	238	α helix
II	311	317	β sheet	9	264	268	β sheet	9	240	245	β sheet
II	323	336	α helix	16	275	289	α helix	13	248	265	α helix
II	342	362	α helix	17	292	320	α helix	14	272	297	α helix
III	365	371	β sheet	10	327	332	β sheet	10	302	307	β sheet
III	373	386	α helix	18	335	347	α helix	15	309	324	α helix
III	388	395	β sheet	11	352	357	β sheet	11	236	332	β sheet
III	400	412	α helix	19	363	375	α helix	16	334	346	α helix
III	418	423	β sheet	12	382	386	β sheet	12	351	354	β sheet
III	426	436	α helix	20	391	400	α helix	17	356	369	α helix
III	440	445	β sheet	13	408	412	β sheet	13	371	375	β sheet
III	446	459	α helix	21	414	422	α helix	18	376	387	α helix
III	463	469	β sheet	14	426	430	β sheet	14	388	392	β sheet
III	478	481	α helix	22					398	402	α helix
III	488	510	α helix	23	446	465	α helix	19	410	439	α helix

Extended Data Fig. 7 | Beta subunit domain structure and residue numbering. Structures colored by domain for **A**) MarK, **B**) NifK, and **C**) DPOR ChlB. **D**) NifK secondary structure and **E**) enumeration of secondary structure based off Kim et al, 1992, Nature[25]. For MarK, cream highlighted cells indicate regions of poor resolution in Cryo-EM structure (Extended Data Fig. 4) and are inferred from AlphaFold 3 model.

A Complementation studies showing MarH, MarD, and MarK are required for Mar activity

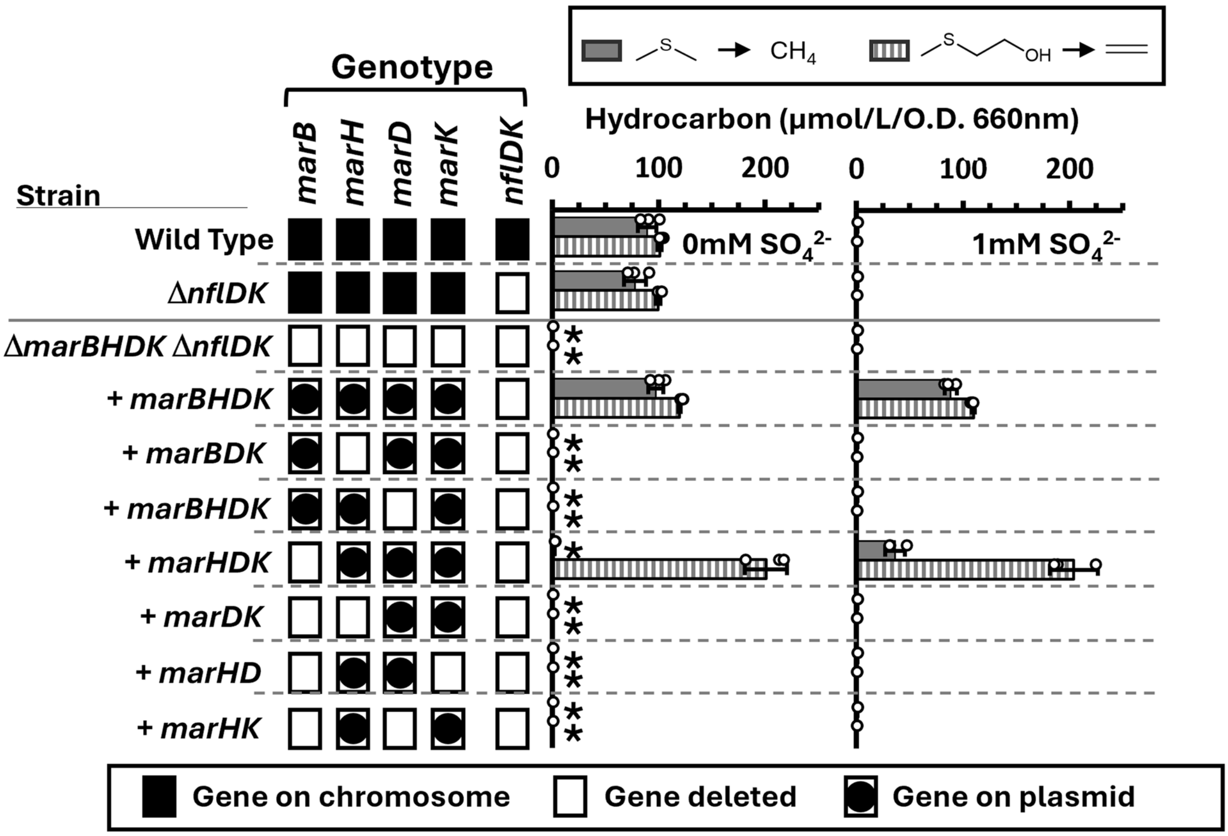

B Complementation studies showing MarS is not required for Mar maturation by MarB or NifB

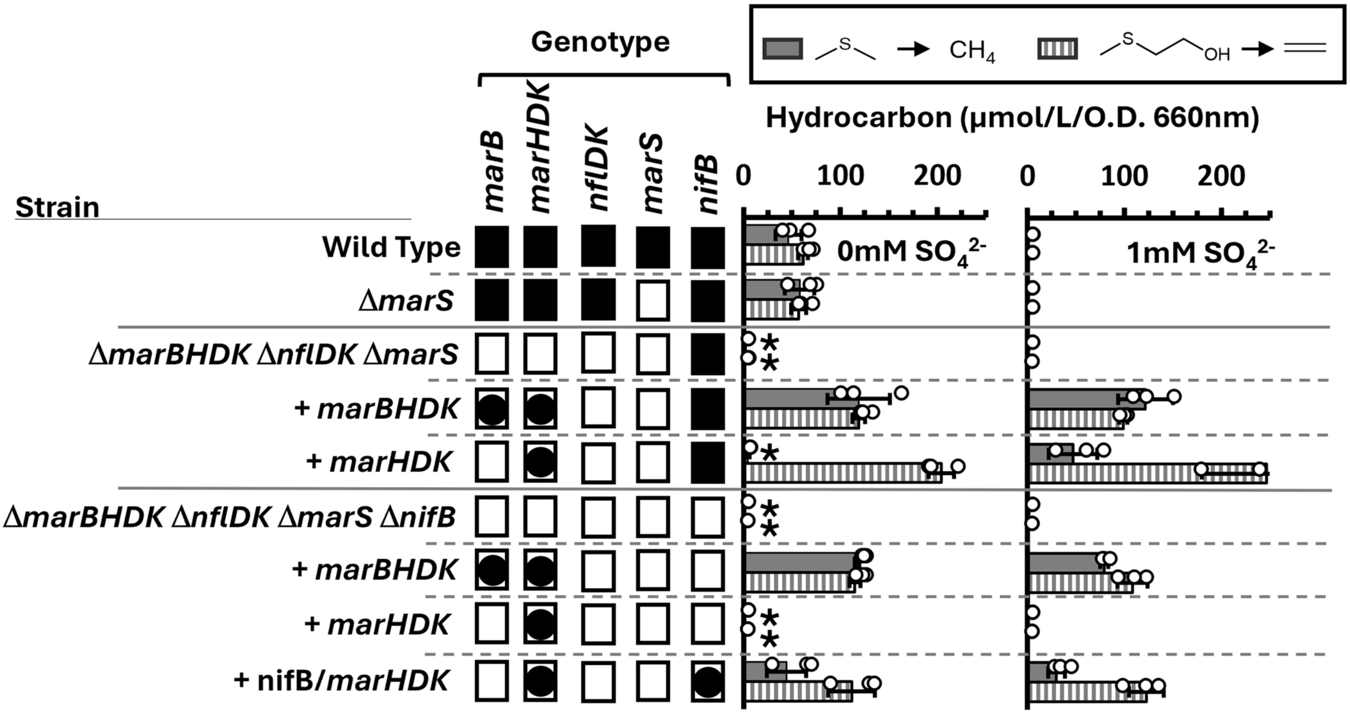

Extended Data Fig. 8 | See next page for caption.

Extended Data Fig. 8 | Genetic requirements for MAR activity. A-B) In vivo MAR cleavage of VOSCs when *marBHDK*, *nflDK, marS* (R. rubrum loci Rru_A3441), and *nifB* are present on the chromosome, deleted, or restored *in trans* from a plasmid. MAR genes on the chromosome are regulated by SalR and expression is repressed by sulfate[5]. MAR and Nif genes on the plasmid are constitutively expressed. g DCW; grams dry cell weight. * indicates strains could not grow on DMS or MT-EtOH as sole S-source. All other strains grew to O.D. 660 nm of 2.0 in 48 hours. All averages and standard deviation error bars in **A**-**B** are for n = 3 independent experiments.

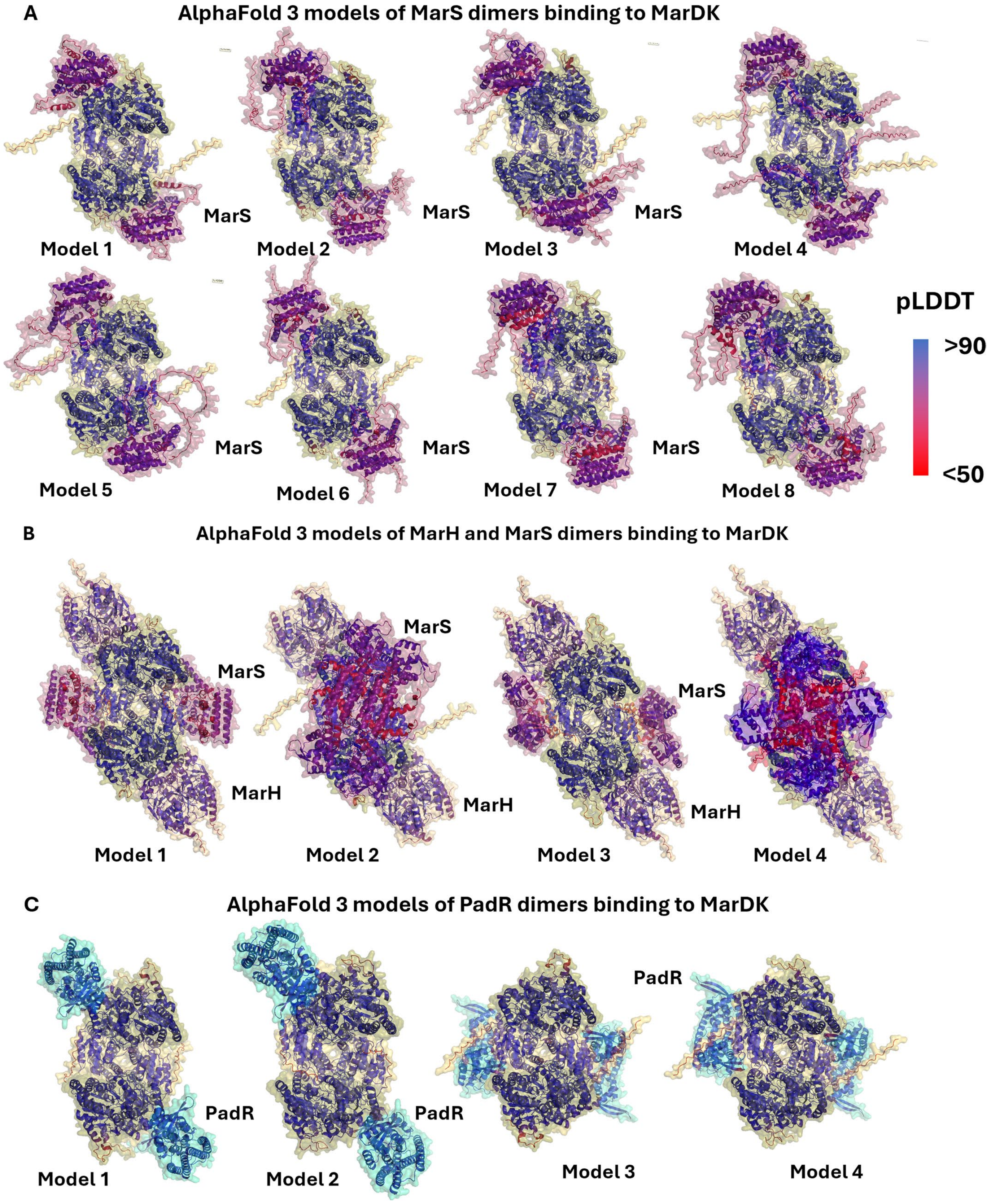

Extended Data Fig. 9 | AlphaFold 3 models of MarH and MarS binding to MarDK. A) Four copies of MarS (NCBI: WP_01139188.1) modeled with a MarDK tetramer (NCBI: WP_011388552.1, WP_011388551.1) shows consistently predicted localization of MarS to the same surface where MarH is predicted to bind. **B**) Four copies of MarH (NCBI: WP_011388553.1) modeled with a MarDK tetramer and two MarS tetramers shows now preferred MarS binding location when MarH is bound. **C**) Two PadR dimers (NCBI: WP_003233588.1) bound to MarDK tetramer. PadR is the winged helix transcriptional regulator for the *Bacillus subtilis* phenolic acid decarboxylase gene operon for which this family of proteins is named and shares 36% sequence identity with MarS.

https://doi.org/10.1038/s41929-025-01425-3

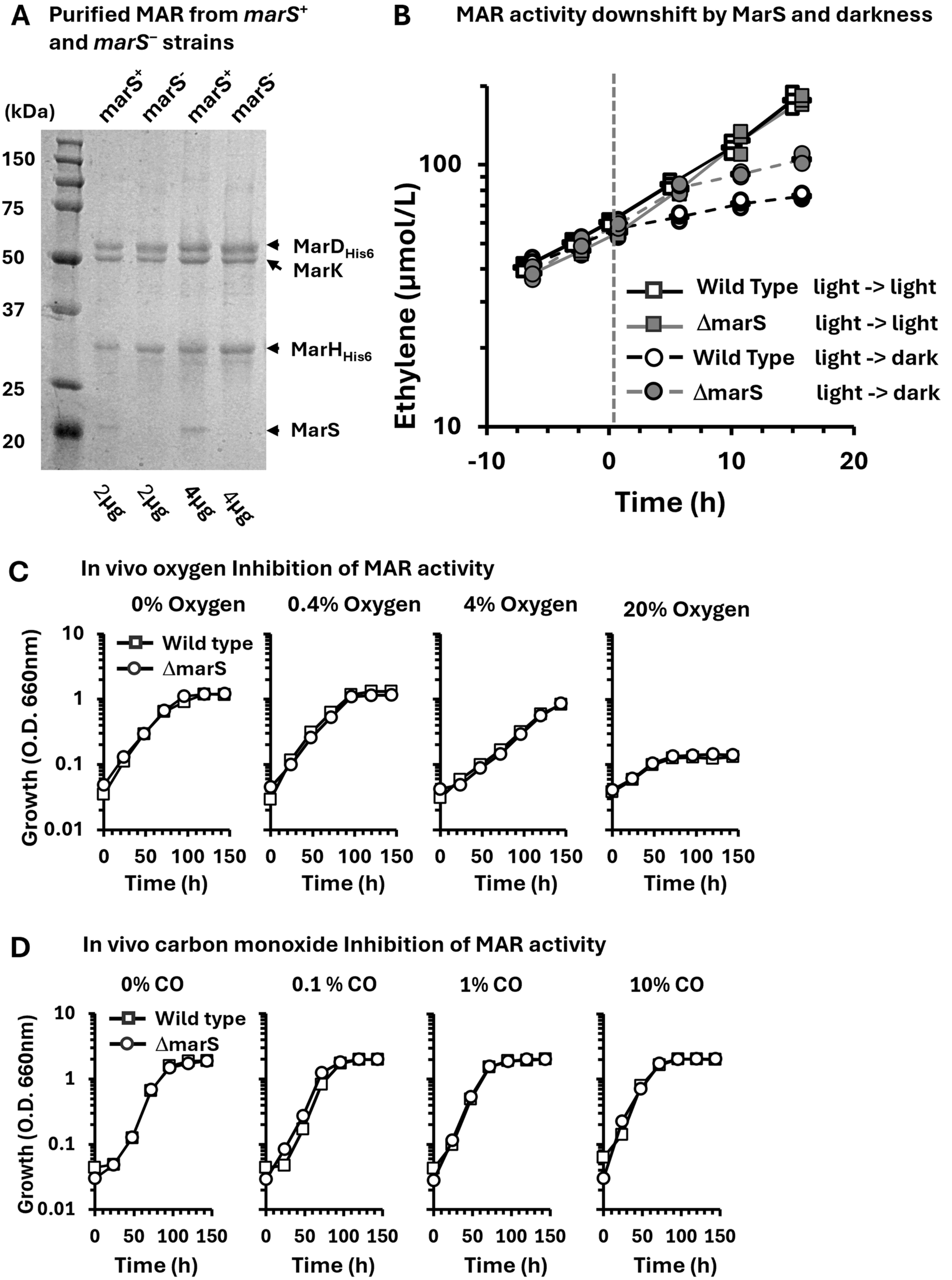

Extended Data Fig. 10 | See next page for caption.

Extended Data Fig. 10 | MarS is involved in sulfate influx and dark switch-off. A) MarHDK with MarS purified by Ni-NTA affinity and DEAE ion exchange chromatography from strain Δ*marBHDK* Δ*nflDK* (*marS*$^+$strain) with MAR overproduction plasmid and MarHDK devoid of MarS purified by Ni-NTA affinity and DEAE ion exchange chromatography from strain Δ*marBHDK* Δ*nflDK* Δ*marS* (*marS*$^{-}$ strain) with MAR overproduction plasmid. Purification experiments were performed on n = 2 independent protein samples with same results. **B**) Ethylene production from 2-methylthioethanol by MAR activity in wild type and MarS deletion strain before and after shift to darkness for n = 3 independent experiments. **C** and **D**) Representative growth curves from n = 2 independent experiments for wild type and MarS deletion strain under phototrophic conditions with varying oxygen and carbon monoxide concentrations.

nature portfolio

Corresponding author(s): J. North (north.62@osu.edu)

Last updated by author(s): 7/17/2024

Reporting Summary

Nature Portfolio wishes to improve the reproducibility of the work that we publish. This form provides structure for consistency and transparency in reporting. For further information on Nature Portfolio policies, see our Editorial Policies and the Editorial Policy Checklist.

Statistics

For all statistical analyses, confirm that the following items are present in the figure legend, table legend, main text, or Methods section.

n/a	Confirmed	
☐	☒	The exact sample size (*n*) for each experimental group/condition, given as a discrete number and unit of measurement
☐	☒	A statement on whether measurements were taken from distinct samples or whether the same sample was measured repeatedly
☐	☒	The statistical test(s) used AND whether they are one- or two-sided *Only common tests should be described solely by name; describe more complex techniques in the Methods section.*
☒	☐	A description of all covariates tested
☒	☐	A description of any assumptions or corrections, such as tests of normality and adjustment for multiple comparisons
☐	☒	A full description of the statistical parameters including central tendency (e.g. means) or other basic estimates (e.g. regression coefficient) AND variation (e.g. standard deviation) or associated estimates of uncertainty (e.g. confidence intervals)
☒	☐	For null hypothesis testing, the test statistic (e.g. *F*, *t*, *r*) with confidence intervals, effect sizes, degrees of freedom and *P* value noted *Give P values as exact values whenever suitable.*
☒	☐	For Bayesian analysis, information on the choice of priors and Markov chain Monte Carlo settings
☒	☐	For hierarchical and complex designs, identification of the appropriate level for tests and full reporting of outcomes
☒	☐	Estimates of effect sizes (e.g. Cohen's *d*, Pearson's *r*), indicating how they were calculated

Our web collection on statistics for biologists contains articles on many of the points above.

Software and code

Policy information about availability of computer code

Data collection	no software was used for data collection
Data analysis	EasySpin Matlab toolbox, CryoSPARCworkflow, alphafold-multimer, ISOLDE in ChimeraX package, MolProbity in PHENIX package, Chai-1

For manuscripts utilizing custom algorithms or software that are central to the research but not yet described in published literature, software must be made available to editors and reviewers. We strongly encourage code deposition in a community repository (e.g. GitHub). See the Nature Portfolio guidelines for submitting code & software for further information.

Data

Policy information about availability of data

All manuscripts must include a data availability statement. This statement should provide the following information, where applicable:

- Accession codes, unique identifiers, or web links for publicly available datasets
- A description of any restrictions on data availability
- For clinical datasets or third party data, please ensure that the statement adheres to our policy

Structural models and electron density maps are available through PDB ID 9D9U and EMDB ID EMD-46680.

Research involving human participants, their data, or biological material

Policy information about studies with human participants or human data. See also policy information about sex, gender (identity/presentation), and sexual orientation and race, ethnicity and racism.

Reporting on sex and gender	N/A
Reporting on race, ethnicity, or other socially relevant groupings	N/A
Population characteristics	N/A
Recruitment	N/A
Ethics oversight	N/A

Note that full information on the approval of the study protocol must also be provided in the manuscript.

Field-specific reporting

Please select the one below that is the best fit for your research. If you are not sure, read the appropriate sections before making your selection.

☒ Life sciences ☐ Behavioural & social sciences ☐ Ecological, evolutionary & environmental sciences

For a reference copy of the document with all sections, see nature.com/documents/nr-reporting-summary-flat.pdf

Life sciences study design

All studies must disclose on these points even when the disclosure is negative.

Sample size	For each experiment, bacteria or proteins are used and thus do not involve a sample size of n. Experiments were performed in biological replicate of n=3 to determine experimental average and standard deviation.
Data exclusions	no data presented in the figures and tables were excluded from the analysis
Replication	Table 1: Averages and standard deviation error bars are for n=3 independent experiments Figure 2: Monographs and chromatograms in B,D-F were conducted n=2 times with same results Fig. 3B,C,D,F) Averages and standard deviation error bars are for n=3 independent experiments. Fig. 3D) Specific activity of MAR with each VOSC substrate obtained by weighted linear regression and standard error calculation from data in (C). Fig. 3E) EPR experiments conducted n=2 times with same results Fig. 6D,E) Averages and standard deviation error bars are for n=3 independent experiments. Fig. 7A,B) Averages and standard deviation error bars are for n=3 independent experiments. Extended Data Fig. 1C) Activity and functional requirements of native MAR activity in the DEAE fraction (B) for n=1 sample Extended Data Fig. 1D,E,F) averages and standard deviation error bars are for n=3 independent experiments Extended Data Fig. 2A,B) Experiments conducted for n=2 samples with same results. Extended Data Fig. 3) Experiments conducted for n=2 samples with same results. Extended Data Fig. 8) averages and standard deviation error bars are for n=3 independent experiments Extended Data Fig. 10A) Purification experiments were performed on n=2 independent protein samples with same results. Extended Data Fig. 10B) averages and standard deviation error bars are for n=3 independent experiments Extended Data Fig. 10C,D) experiments were performed on n=2 independent protein samples with same results Suppl. Fig. 4) MarH oxidation states were performed for n=2 independent experiments with same results
Randomization	For all bacterial experiments, single initial cultures for each experimental replicate were grown and then split between the control and all treatment groups for each experiment.
Blinding	Blinding was not relevant as all experiments were performed and data immediately obtained for bacterial and protein samples that can visually be distinguished by eye by an investigator.

Reporting for specific materials, systems and methods

We require information from authors about some types of materials, experimental systems and methods used in many studies. Here, indicate whether each material, system or method listed is relevant to your study. If you are not sure if a list item applies to your research, read the appropriate section before selecting a response.

Materials & experimental systems

n/a	Involved in the study
☒	☐ Antibodies
☒	☐ Eukaryotic cell lines
☒	☐ Palaeontology and archaeology
☒	☐ Animals and other organisms
☒	☐ Clinical data
☒	☐ Dual use research of concern
☒	☐ Plants

Methods

n/a	Involved in the study
☒	☐ ChIP-seq
☒	☐ Flow cytometry
☒	☐ MRI-based neuroimaging

Plants

Seed stocks	N/A
Novel plant genotypes	N/A
Authentication	N/A